A computationally efficient methodology to simulate hybrid bolted joints including thermal effects

José M. Guerrero[a,*], Aravind Sasikumar[a], Jordi Llobet[a], Josep Costa[a]

[a]*AMADE, Polytechnic School, Universitat de Girona, Campus Montilivi s/n, E-17003 Girona, Spain*

Abstract

Carbon-aluminium bolted assemblies are difficult to simulate because of the complex phenomenology involved (contact, friction, preload and thermal expansion). Therefore, accurate but computationally feasible methodologies are necessary. We propose two simplified methodologies, one based on continuum shell elements and the other on conventional shells, and compare them with a full 3D solids model. The two cases explored are a single-lap shear coupon with one bolt, and a hybrid wingbox subcomponent with 46 bolts. The effect of temperature jumps on the bolt preloads are explored. Results show that the continuum shell model presents the best trade-off between accuracy and computational cost.

Keywords: Hybrid structures, Bolted joints, Computational modelling, Thermal loading, Aircraft structure, Composite laminates, Finite element method

1. Introduction

Several modern aircraft combine Carbon Fibre Reinforced Polymer (CFRP) components (for example, skins) with aluminium parts (ribs, etc.) [1]. The common approach to assemble CFRP-aluminium elements is to use bolted joints due to their high stiffness and strength as well as to the ease of disassembly for inspection and repair [2–5]. However, the very different thermal expansion coefficients of aluminium and CFRP, cause thermal stresses during aircraft operation (temperature differences between a landed plane and one a flying can reach 140 ºC). This differential expansion/contraction affects the performance of the bolted joint as it modifies, for example, the clamping force of the bolt [6, 7].

*Corresponding author. Tel.: +34 972 41 88 17.
Email address: josemanuel.guerrero@udg.edu (José M. Guerrero)

A reliable design, therefore, needs to account for these thermal effects. The few studies on hybrid bolted joints under thermal loading have focused on the effect temperature has on the bearing strength and damage modes of the joints [6, 7]. In any case, the numerical simulation of a bolted joint is challenging because of the overlapping effects of several parameters such as the bolt-hole clearance, the bolt clamping force, the friction sliding between surfaces, in addition to the above-mentioned thermal effects [2, 4, 7–12].

Current methods to estimate the behaviour of bolted joints can be categorized in [12]: analytical methods [4, 8, 13, 14], the stiffness method [12, 15–18], and the finite element method [2, 3, 5, 18–32]. Analytical methods consist of a closed-form solution of a model where bolts and components are represented by a series of springs and masses [27]. These methodologies are computationally efficient and relatively simple, but they only partially represent the behaviour of the bolted assembly, and fail to accurately capture the failure of the joint [30]. Similarly, in the stiffness method the bolts are modelled as beams, while the components are considered as springs. Thus, these models are still computationally efficient and can reproduce the behaviour of the joint in a more accurate way than analytical models can [12]. Nonetheless, while only three-dimensional (3D) Finite Element Models (FEM) can accurately reproduce the behaviour of the joint at the vicinity of the bolt, the interaction between all components, as well as the through-thickness stresses, this is at the expense of being computationally costly [2, 30].

One of the earliest 3D FEMs was developed by Ireman [19], and takes into account many features such as contact, friction, preload, bolt type (countersunk or protruding) and clearance. The model was subsequently refined by Tserpes *et al.* [22]. Later, McCarthy *et al.* [24] developed a 3D FEM of a composite single-lap shear test with one single bolt, solving contact issues, to ultimately concentrate on bolt clearance [25].

Stocchi *et al.* [2] presented a more advanced 3D FEM of a single-lap shear composite bolted joint, with titanium countersunk fasteners. The model considered contact between all interfaces, friction, clearance and, unlike previous models, it also included part of the thread of the bolt. These authors conducted a parametric study to clarify the importance of the bolt clamping force, coefficient of friction and clearance, and reached a good agreement with experimental results. More recently, Mandal *et al.* [30], with a 3D FEM, investigated the failure of composite bolted joints taking into account delamination, fibre and matrix tensile failure, compression and shear failure. Their study attained multi-bolt composite joints with varying preloads and bolt diameters. Moreover, Shan *et al.* [33] presented an FEM to predict the fatigue failure of a composite-aluminium double joint. The model correlated well with experimental results.

In search for a proper trade-off between computational effort and model reliability, simpler models have also been reported. Ekh and Schön [27] developed a 1D FEM capable of capturing bolt clamping, clearance and friction. Similarly, other authors used 2D FEM to simulate the plates as solid-shell elements or shells [21, 34, 35]. These simple models, although computationally efficient, are not able to capture through-thickness effects [2, 23]. Alternatively, user-defined elements can be developed to take into account the presence of the bolt, washer and nut without modelling them physically [28, 36–38]. Gray *et al.* [28] presented a user-element able to capture the full non-linear load-displacement behaviour of composite bolted joints. Belardi *et al.* [36–38] developed a user-defined finite element, which represents the elastic behaviour of the region comprising the bolted joint, and a small portion of the surrounding composite plates. The model was validated against experimental data [38]. The downside of these methods is that such user-defined formulations need to be implemented by the user in the commercial finite element software.

Although 3D FEM can take into account the main physics involved in bolted joints (frictional contacts, transverse stresses, thermal effects, etc.), simulating a large structure containing hundreds of bolts is unfeasible [12]. It is therefore imperative to simplify the FEM. Firstly, the 3D parts joined by the bolt can be simplified by either solid-shell elements, or traditional shell elements [21, 34, 35]. Secondly, the 3D bolt can be replaced by beam elements, a coupling, a rigid body or can even be removed, among others [4, 28, 35, 39]. Likewise, some contact interfaces may be modelled with an adequate multi-point constraint [35]. It is yet unclear, however, to what extent a simplified model can capture the response of a large hybrid structure with many bolts. To clarify this point, in this paper we propose a comparison of a detailed 3D model with two simplified methodologies: one using continuum shells and the other conventional shells. In both cases the bolts are modelled as beams. The considered case studies are a single-lap shear coupon and a complex wingbox subcomponent assembly. In view of the lack of published knowledge on this issue, we specifically concentrate on the influence thermal loading has on the bolted hybrid assembly.

As a result of this investigation, we claim that an FEM based on continuum shells and beams is suitable to reproduce the mechanical behaviour of a large hybrid structure, including the effects caused by thermal dimensional changes. This work is part of an ongoing EU Cleansky-2 project 'INNOHYBOX', developed within the consortium of Dassault Aviation, AMADE research group from the University of Girona, the technological Centre EURECAT and the company SOFITEC, with the global objective of experimentally and numerically analysing an aircraft hybrid wingbox structure subjected to thermo-mechanical loads.

2. Methodology

In this section, we describe the two simplified methodologies as well as the high fidelity 3D model, each of them taking into consideration the most relevant phenomena in the hybrid bolted joint (contacts, friction, bolt preload and thermal expansion). Any form of damage or plasticity is ignored, although these effects could be included in a more refined model. Finally, this work is carried out using the Abaqus 6.14 finite element program [40], with an implicit integration scheme. Our approach makes use of tools that are directly available in the commercial software, so that our methodology can be easily adopted by the industry.

2.1. Benchmark: 3D solids

In this approach, 3D solid elements are used to model all the parts of the assembly, being therefore the most accurate method used in this work. To facilitate the explanation, let us assume a hybrid assembly, comprised of two plates with different material properties, joined by a countersunk bolt, see Fig. 1a. The bolt, washer and nut (of same diameter as the washer) are considered to be a single part in order to minimise the contact surfaces [7]. Moreover, the thread is not physically modelled. Instead, the bolt shaft is considered as an axial revolution, where the diameter of the bolt is taken as the diameter of the corresponding thread [30]. All these parts are meshed with 3D solid elements of type C3D8R (an eight node 3D brick element with reduced integration, see Fig. 1a).

[Figure 1 about here.]

Sliding and friction between the contacting surfaces is taken into account by assigning the following contact interactions: (i) between the two plates, (ii) between the entire bolt shaft and the hole of the plates, and (iii) between the washer and the bottom plate, see Fig. 1b. These contact interactions are simulated by means of the surface-to-surface contact algorithm of Abaqus/Standard, using finite sliding formulation. The tangential behaviour of the contact follows a penalty friction formulation, whereas the normal behaviour is given by hard contact [40]. Finite clearances can be included between the bolt and the hole of the plates.

The preload of the bolt is simulated using the Abaqus 'bolt load' feature [2, 30, 40]. The middle surface of the bolt is selected, and a preload force is assigned to the nodes in it (Fig. 1c). In this way, Abaqus progressively adjusts the length of the underlying elements of the selected nodes along the bolt axis until the sum of the reaction forces of the nodes in the surface matches the user-defined preload force. This adjustment is kept fixed in the next steps of the simulation, so that the preload is maintained and the bolt can act as a deformable part when other loads are applied. For more information on this, the reader is referred to Abaqus documentation [40].

To model thermal loading, we specify the final temperature and amplitude change in a pre-defined field option. The temperature difference, the coefficient of thermal expansion of the materials and the geometry determine the expansion or contraction in all three directions for each element.

2.2. Continuum shells and beams

The plates are meshed with Continuum Shells (CONTS) of type SC8R (an eight node quadrilateral continuum element with reduced integration). This kind of element technology has only displacement degrees of freedom like solid elements, but their kinematic formulation mimics that of conventional shell elements, being, therefore, in-between solid and shell elements [40]. Thus, the mesh of the plates would be akin to the one shown in Fig. 1a. Notice that, like with 3D solids, the CONTS also allow a countersunk fastener shape to be taken into account in the plates.

To model the bolt, we use beam elements of type B31 (2-node linear beam). Unlike 3D solids, where a complex section can be considered for the bolt (such as a countersunk), in this case the bolt is considered to have a cylindrical section with diameter equal to that of the bolt thread along all its length. Given that the section of the beam is 'virtual' (i.e. there is physically no section present), a cylindrical surface with a diameter equal to that of the bolt is added to physically represent its diameter. Such a surface is meshed with Surface Elements (SFM) of type SFM3D4R (4-node quadrilateral surface element with reduced integration), see Fig. 2a. These surface elements are connected to the beam by means of a tie constraint, where the beam nodes are selected as the master and the SFM nodes as the slaves, Fig. 2b. The SFM can be understood as a surface of nodes in the space, with no inherent stiffness and no material properties, which move according to the displacements and the rotations of the beam, without storing elastic energy [40].

[Figure 2 about here.]

Unlike 3D solids, the washer and nut are removed from the model. To take into account their presence in a simplified manner, a circular partition with diameter equal to that of the washer is created in the bottom plate where the washer would be in contact. A tie constraint is defined where the bottom node of the beam is selected as the master and the circular partition of the bottom plate as the slave, Fig. 2c. Thus, unlike 3D solids, the contact between the washer and the plate (illustrated in Fig. 1b) is omitted. Likewise, another tie constraint is used for the head of the bolt, where the top nodes of the beam are selected as the master and the countersunk surface of the top plate as the slave, Fig. 2d. Consequently, the contact between the bolt head and the top plate is also omitted.

Contact interactions are assigned to: (i) between the two plates, and (ii) between the SFM surface and the hole of the plates, see Fig. 2e. Like with 3D solids, a finite sliding algorithm is used, with a penalty friction formulation and hard contact. For the contact between the SFM and the hole, the SFM is selected as the master and the surface of the hole of the plates as the slave. Therefore, the SFM is added just to facilitate the modelling of the contact between the bolt and the hole. Without the SFM, convergence becomes more complicated since contact has to be applied between the beam's virtual diameter (which is not physically present into the model) and the hole. With this approach instead, the contact is modelled between the SFM and the hole in an easier manner.

The preload of the bolt is again simulated using the Abaqus bolt load feature, by applying a preload force onto the middle element of the beam (Fig. 2f). Finally, thermal loading is modelled in the same way as explained in Section 2.1. Nonetheless, it should be noted that, unlike 3D solids, CONTS assume plane stress conditions, and therefore the through-thickness behaviour only is estimated.

2.3. Conventional shells and beams

In this model, the plates are meshed with Conventional Shells (CONVS) of type S4R (a four node thin or thick shell element with reduced integration). As a difference from CONTS and solid elements, these kinds of elements have displacement and rotational degrees of freedom, as well as a virtual thickness, being, therefore, much simpler and computationally cheaper. Notice that, unlike 3D solids and CONTS, CONVS do not allow a countersunk shape to be included in the plates, since only a reference surface along the thickness is considered. To physically represent the hole of the plates along their entire virtual thickness, a cylindrical surface of a diameter equal to that of the hole is added. This surface is meshed with elements of type SFM, see Fig. 3a. A tie constraint is defined between the hole edge of the shells (as master) and the entire SFM that represents the hole (as slave), see Fig. 3b. Thus, this SFM does not have any material properties, and will simply deform together with the hole of the shells. It is also worth mentioning that, as illustrated in Fig. 3a, the shell surface is placed at the top for the top plate, and at the bottom for the bottom plate. This is done for convenience, since it will facilitate the definition of the interaction properties as will be clarified later.

[Figure 3 about here.]

Like with CONTS, the bolt is modelled with beam elements together with SFM to represent its diameter, with both being tied, see Fig. 2a-b. In the same way, to represent the washer-nut, the bottom node of the beam is tied with a circular partition with a diameter equal to that of the washer at the bottom plate (Fig. 3c). Likewise, the top nodes of the beam are also tied with a circular partition of a diameter equal to that of the countersunk in the top plate, see Fig. 3d. These two ties are created by excluding the shell virtual thickness. As a consequence, the virtual thickness of the shells is not tied to the beam. This is the reason why the shells are not placed at the middle surface.

Contact interactions are applied to: (i) between the virtual thickness of the two shell plates, and (ii) between the SFM surface of the beam and the SFM surface of the hole of the plates, see Fig. 4. Like previously, the finite sliding algorithm is used, with the penalty friction formulation and hard contact. For the contact between the two SFMs, the bolt SFM is taken as the master and the SFM of the hole of the plates as the slave. It should be clarified that, the SFM of the hole is needed to properly capture the contact between the bolt and the hole, since contact with the shell virtual thickness in the out-of-plane direction is not possible in Abaqus. Therefore, this explains the need to have 2 SFMs: one to physically represent the diameter of the beam, and another to physically represent the diameter of the hole of the plates. With the approach proposed, the contact in the thickness direction can be partially captured. Like with CONTS, the contact between the washer and the plate, and between the head of the bolt and the top plate are omitted.

[Figure 4 about here.]

The preload of the bolt is simulated as explained in Section 2.2, whereas thermal loading is also modelled as in Section 2.1. However, like CONTS, CONVS consider plane stress conditions, as well as a reference surface for all the thickness, and therefore the out-of-plane behaviour is heavily simplified.

3. Case studies

We compared the fidelity and computational cost of the models described above in two cases: a CFRP-aluminium Single-Lap Shear (SLS) coupon with one bolt, and a wingbox subcomponent with an element of an aluminium rib in between carbon skins and spars, including 46 bolts.

3.1. Coupon level: single-lap shear test

The SLS test consists of a hybrid assembly between CFRP and aluminium plates joined by a countersunk fastener. The coupon includes doublers bonded to each plate to counteract the moments in the assembly. Fig. 5 shows the geometrical details and the model with 3D solids, while Fig. 6 depicts the models with CONTS and CONVS elements. Most of the specimen dimensions are in accordance with the ASTM standards D5961/D5961-M [41], whereas the bolt dimensions follow the NAS-1153 standard. The bolt-hole clearance is set at 0.06 mm, in agreement with the range found in aerospace structures of between 0.05-0.15 mm [9, 42].

[Figure 5 about here.]

[Figure 6 about here.]

The material properties can be found in Table 1. The bolt, washer and nut are made of steel. All materials are assumed linear elastic and CFRP is considered orthotropic, with 40 plies. The coefficient of thermal expansion, CTE, is considered isotropic for metals and is given in the three directions for CFRP. The laminate stacking sequence is defined in Abaqus using the 'composite layup' feature [40]. Three integration points are considered for each ply of the laminate. All contact interfaces have a friction coefficient of 0.315, as determined experimentally. Moreover, for the CONVS model, a tie constraint holds the plates and doublers together. In contrast, the 3D solids and CONTS models do not need this tie constraint since the plate and doubler are modelled as a single part. We omitted the weight of the assembly.

[Table 1 about here.]

The global mesh size in the plates is 1 mm, which is refined to 0.75 mm around the hole region. For the 3D solids and CONTS models, this leads to ten elements through the thickness for the CFRP plate, and eight for the aluminium one. Therefore, each element of the CFRP laminates contains four plies. The bolt has a mesh size of 0.3 mm. A parametric study was conducted to confirm the validity of these mesh dimensions. In addition, the same mesh size is employed for each of the three numerical approaches, so that the comparison between them is fair. The CONTS model reduces the number of elements with respect of the 3D solids model by 17 %, while the CONVS model is by 86 % (Table 2).

[Table 2 about here.]

The SLS simulation consists of the following three steps:

- Step 1: preload. A preload force of 6000 N (corresponding to a torque of approximately 4 N·m, which is a standard value) is applied to the bolt, as described in Section 2. The two sides of the assembly are clamped during this step (see Fig. 7a). The temperature of the assembly is set to room temperature (25 °C).
- Step 2: thermal. After the bolt preload, we apply a thermal step (either positive or negative). The positive involves a temperature jump from 25 °C to 90 °C. The negative from 25 °C to -55 °C. The two sides of the assembly are also clamped throughout this step (see Fig. 7b).
- Step 3: tension. A longitudinal displacement of 0.65 mm is applied to the left side of the assembly to simulate the shearing of the joint. The right side of the assembly is clamped during this step (see Fig. 7c).

[Figure 7 about here.]

3.2. Structural level: wingbox subcomponent

The wingbox subcomponent consists of two CFRP spars, two CFRP skins and one aluminium rib, according to the geometry sketched in Fig. 8 for the 3D solids model and in Fig. 9 for CONTS and CONVS models. The rib is connected to the upper and bottom skins with 2 bolts each, and to each spar with 3 bolts. Skin and spars are joined by 36 bolts (9 at each contacting surface). So, the assembly contains 46 bolted joints, see Fig. 8. The bolt dimensions and bolt-hole clearance are the same as in the SLS model.

[Figure 8 about here.]

[Figure 9 about here.]

Materials and material properties are identical to the ones described in the SLS model (Table 1). The CFRP skins and spars have 60 and 26 plies, respectively, and are modelled as in Section 3.1. The weight of the structure is accounted for by means of the gravity feature of Abaqus [40], which applies a load in the gravity direction to each element of the model according to the element's material density and volume.

To represent the boundary conditions of the experiments to be performed in the framework of the INNOHYBOX project, the four corners of the subcomponent are placed on four perfectly rigid surfaces (referred to as floors). These floors have the displacement in the three directions constrained (see Fig. 10). However, placing the structure just on top of the floors does not avoid motion of the assembly in all directions. Hence, four fictitious frames of very low stiffness (0.1 GPa) are tied to each corner of the bottom skin (see Figs. 8 and 9). Half of the bottom surface of the four frames is clamped (Fig. 10). This approach permits the bottom skin to deform freely under temperature excursions in all directions, as no boundary conditions are applied onto it, while the compliant frames imped rigid body motion. Other boundary conditions without floor or frames did not produce realistic results or had convergence issues.

We assigned contact interactions between: i) the skins and the rib, ii) the spars and the rib, iii) the skins and the spars, iv) the bottom skin and the floor, v) the frames and the floor and vi) the bolts and their holes. All contacts follow the description given in Section 2. The friction coefficient for CFRP-aluminium/steel and aluminium-steel interfaces is 0.315 and 0.126 for CFRP-CFRP contacts. These values were obtained experimentally.

The global mesh size in the rib, skins and spars is 3 mm, which is refined to 0.5-0.75 mm around the hole regions. Four elements through the thickness are used for the 3D solids and CONTS. Therefore, each element of the composite laminates contains several plies. The bolts have a mesh size of 0.3-0.5 mm. The same mesh dimensions are used for the three finite element approaches to ensure a fair comparison between them. CONTS and CONVS models reduce by 18 % and 48 %, respectively, the number of elements relative to the 3D solids model (Table 2).

The simulation consists of the following two steps:

- Step 1: preload. A preload force of 6000 N is applied to all 46 bolts, as described in Section 2. The temperature is set to room temperature (25 °C) to all the wingbox subcomponent (thermal effects are not applied to the frames and floors). In addition to this, the gravity is also applied at the beginning of this step and maintained for the rest of the simulation, see Fig. 10a.
- Step 2: thermal. We investigate the effect of two thermal steps. A positive jump, between 25 °C to 90 °C, and a negative one, between 25 °C to -55 °C (Fig. 10b).

[Figure 10 about here.]

4. Results

4.1. Coupon level: single-lap shear test

Figs. 11a and 11b show the evolution of the clamping force during the three stages of the SLS simulation: preload up to 6 kN, thermal jump (either positive or negative) and tensile test. The three models result in the same evolution of the clamping force during the preload step. The response during the thermal step (time 1-2 s) depends on the modelling approach and the thermal jump sense. In a positive thermal step (Fig. 11a), the clamping force increases progressively for the CONTS and the 3D solids, both giving qualitatively the same result. Oppositely, it decreases in the CONVS model. The reverse trend occurs for a negative thermal step (Fig. 11b): the clamping force decreases for the CONTS and the 3D solids models, but increases for the CONVS one.

[Figure 11 about here.]

The load displacement curve during the tensile test for a positive thermal jump (Fig. 11c) exhibits three stages for the 3D solids and CONTS models. The initial stiffness decreases from point A (displacement of 0.2 mm) to point B (0.4 mm), above which the stiffness is practically recovered. While 3D solids and CONTS models coincide in this response, the CONVS model only shows one change in slope, occurring at lower displacements than point A. For the negative thermal step, only one stiffness stage occurs for the entire tensile response (Fig. 11d). The 3D solids and the CONTS models are again in good agreement while the CONVS model presents a significant lower stiffness.

Regarding the clamping force during the tensile test after the positive thermal jump, this follows an initial plateau after which it decreases because the two plates start to slide (Fig. 11a). In the test after the negative thermal step (Fig. 11b) the clamping force decreases continuously, since the two plates slide from the very beginning. The clamping force evolution is similar for the three methodologies, although the CONVS differs from the other two because of its wrong prediction during the thermal loading.

In summary, the response of the bolted SLS coupon is highly influenced by the temperature jump. The computational time using 20 cpus, was around 38 min for the 3D solids, 33 min for the CONTS and 17 min for the CONVS (Table 2).

4.2. Structural level: wingbox subcomponent

Fig. 12 illustrates the displacements in the subcomponent for the positive and negative thermal jumps. Overall, the larger expansion/contraction of the ribs during the thermal jump causes the spar and the skin to bend accordingly. This is qualitatively captured by the three models.

The 3D solids and the CONTS models predict very similar displacement contours. In contrast, the CONVS model predicts much lower maximum displacements (for the positive thermal jump it predicts 0.20 mm compared with 0.28 mm and 0.31 mm for the CONTS and 3D solids models, respectively) and the displacement contour is also a bit different. The CONVS model shows lower displacement towards the centre of the rib (in the vicinity of the central hole). Moreover, for the negative jump, the displacement in the top part of the centre hole of the rib for the CONVS model is lower than in 3D solids and the CONTS models.

[Figure 12 about here.]

Fig. 13 shows the clamping force of all bolts in the subcomponent during the preload and thermal step for the three models. Bolts are grouped according to the elements they join: rib-skin, rib-spar and skin-spar. With a positive thermal step (Fig. 13a-c), the clamping force increases considerably for the CONTS and the 3D solids models, both giving similar results, while it decreases in the CONVS model. The negative thermal step (Fig. 13d-f) shows the opposite trend: it decreases for the CONTS and the 3D solids models and increases for the CONVS one. These tendencies coincide with the simulation of the SLS coupon (see Section 4.1). It must be emphasized that the clamping force in the rib-skin bolts decreases by around 66 %.

[Figure 13 about here.]

In addition, we verified that the average bolt longitudinal stress equals the clamping force divided by the bolt cross-section, and thus, the stress follows the same trend as the clamping force. Interestingly, this indicates that bolt yielding may occur at the end of the positive thermal jump because the bolt stress reaches 450 MPa. It is also worth mentioning that all the bolts in each contact region present similar clamping force and stress.

The Von Mises stress in the rib is low overall, about 0-50 MPa, except around the bolted holes where it ranges between 50-280 MPa, depending on the simulation methodology and sense of the thermal jump (Fig. 14). The three models show similar contours and indicate the same critical areas: the bolt holes, the corners and the rib centre hole. For the positive thermal step, the CONTS model shows slightly larger peak values in specific regions around the holes, where tie constraints are applied. For the negative thermal jump, the CONTS and CONVS models produce higher stresses in the holes than the 3D solids model.

[Figure 14 about here.]

In line with the rib, the maximum principal stress is low for most of the skins and spars, around 10-100 MPa (Fig. 15), with larger peak values all over the holes. In the countersunk area of the holes, the 3D solids and the CONTS models agree on the contours and predict peak stresses between 100-600 MPa, although the CONTS model predicts larger peaks. In contrast, in the CONVS model, the most critical area is located in elements surrounding the holes of the top skin. In general, the stresses in the skins are larger than in the spars.

[Figure 15 about here.]

To further illustrate the differences between the models, Fig. 16 shows the stresses along a path in different critical areas, mainly the rib central axis, the rib connection with the spar, and the skin-to-rib bolted joints. In line with the previous results, the CONTS model is reasonably close to the 3D solids, while the CONVS model prediction is less accurate. The models diverge in the local areas where the stresses are higher, which occur in the bolted joints. In such locations, the relative error predicted by the simplified models can go up to 75%.

[Figure 16 about here.]

Finally, the computational time using 20 cpus, was around 10 hours for the 3D solids model, 2 hours and 35 min for the CONTS model, and around 5 hours for the CONVS one, see Table 2.

5. Discussion

In the previous sections, we have illustrated the feasibility to simulate, in a computationally efficient manner, a subcomponent with tens of bolts, while still accounting for their rich phenomenology: thermal induced variations of the clamping force, sliding, bolt-hole contact, etc. However, CONTS and CONVS models performed differently as we will discuss in this section.

To begin with, the bolt preload can be correctly introduced into the three simulation methodologies, which proves that beam elements can efficiently substitute 3D solid elements for that purpose.

Temperature jumps alter the clamping force severely, see Figs. 11a, 11b and 13. To further illustrate the change of preload with temperature in a more global manner, Fig. 17 shows the percentage change of preload with respect to the temperature jump for the SLS and the subcomponent, and for each numerical approach. The preload variation with temperature is similar for the SLS and subcomponent joints, although the absolute values are different for each bolted joint due to the differences in geometry and material. The results provide a global map of the expected preload change with temperature, which can be quite severe. For instance, in the rib-skin contact (Figs. 13d and 17b) it decreases by around 66% (a larger negative thermal step could even cause a null clamping force, leading to the separation of the assembly). The reason lies in the CTE of aluminium and CFRP (in the thickness direction) being larger than that of steel. In a positive thermal jump, aluminium and CFRP expand more in the thickness direction than the bolt, pushing it to elongate and thus, leading to an increase in the clamping force. If the thermal jump is negative, the increased contraction of aluminium and CFRP reduces the clamping force (Figs. 12 and 17).

The variations in the clamping loads are relevant to industrial applications since they can lead to early bolt yielding, or joint separation, depending on the thermal jump sense. These trends are properly captured by 3D solids and CONTS models. However, the poor performance of the CONVS model relates to its incapability to take into account the out-of-plane thermal expansion of the plates. Basically, the virtual thickness of the CONVS does not expand or contract with temperature with the following implications: In the positive thermal step, the beam (simulating the bolt) expands, while the CFRP and aluminium plates do not. So, the clamping force decreases instead of increasing. The opposite occurs with a negative thermal step. Hence, neglecting the out-of-plane deformation can lead to incorrect predictions of the joint behaviour [2, 30]. For a proper performance of the CONVS shell model under temperature jumps, it would be necessary, at least, that the virtual thickness of the shell elements vary with temperature. Finally, the agreement between the 3D solids and the CONTS models proves that replacing the washer with a tie constraint is a reasonable simplification.

[Figure 17 about here.]

The tensile test of the SLS coupons that experienced a positive thermal jump shows several stages in stiffness, Fig. 11c, as a consequence of the combination of bolt-hole contact and friction. At the start of the tensile test, the bolt is rotated clockwise (Fig. 18a) due to the expansion of the materials during the previous positive thermal jump. Hence, from the start of the test to point A, the bolt is in contact with the hole, leading to a large stiffness. In between points A and B, the plates start to slide due to the introduced shear and the bolt rotates and bends anti-clockwise, so the bolt stops contacting the plates (except for the head of the bolt that is entirely contacting) and the stiffness of the joint decreases (Fig. 18b). After point B, the bolt bends anti-clockwise and contacts again with the plates (on the opposite side to the one was touching at the beginning of the test, see Fig. 18c). Therefore, the stiffness of the joint increases again to a similar value to the one at the beginning of the test. This kind of response can also be observed when no thermal loading is applied [2]. The reason why the CONVS model only shows two stiffness stages during the positive thermal step, is because the bolt does not bend as much anti-clockwise, and thus, the contact with the plates at the end of the test is still slipping, but not sticking (Fig. 19). Consequently, the third stiffness stage does not occur.

[Figure 18 about here.]

In contrast, when the assembly is cooled, the load displacement curve grows monotonically, with no relevant change in stiffness (Fig. 11d). This is because the bolt remains in contact with the plates for all the simulation (Figs. 18d-e) and the plates slide from the very beginning since the force at the start of the tensile step is already large (Fig. 11d). It is worth mentioning that the very high force values seen in Fig. 11c-d may not be realistic due to the omission of damage. Further to this, we note that when a positive thermal step is conducted before the tensile loading, a negative compressive force has already appeared before the start of the tensile step (Fig. 11c). This is because, during the positive thermal step, the whole joint expands. Since the assembly is clamped at the ends (see Fig. 7), a negative reaction force appears at the joint ends [43]. Hence, the tensile step does not start with null force. The reverse occurs when a negative thermal step is applied prior to the tensile step, since in that case, the joint tries to compress during the thermal jump, causing a positive reaction force (Fig. 11d).

[Figure 19 about here.]

The agreement of the CONTS and 3D solids models on the simulation of the SLS coupon proves that the CONTS model is a reliable approach. Oppositely, the CONVS model is quite off from the other two models, especially with a positive thermal step. The reason is due to the fact that the kinematics of conventional shell elements do not account for the through-thickness deformation/expansion of the plates. Besides, the plates are modelled with a representative surface, which means that the contact between the bolt and the plates all along the thickness cannot be captured. Although this limitation was mitigated by adding surface elements to partially capture the bearing contact between the bolt shaft and the plates, the results indicate that the model does not reproduce the physics of the problem precisely. Even though the CONTS elements assume plane stress conditions, such a model considers multiple elements through the thickness and captures the through-thickness behaviour in a simplified manner.

Regarding the wingbox subcomponent, the three methodologies predict the same qualitative deformed shape of the assembly (Fig. 12). The displacement contour in the CONVS model is different because of the inability to capture the out-of-plane behaviour, that is, the thickness deformation and the contact along the thickness.

As illustrated in Fig. 14, the Von Mises stress contour in the rib is qualitatively similar for all methodologies regardless of the thermal jump. The peak stress next to the bolt holes is larger in the CONTS and CONVS models because of the tie constraints between the beams and the rib, which restrict the relative motion and thus increase the stress. However, this only occurs in very local areas, so in qualitative terms the three approaches are similar, see Fig. 16. Likewise, the maximum principal stress contour in the skins and spars (Fig. 15) is qualitatively similar for all methodologies. The peak values are different and located in distinct places: the CONVS model predicts lower peak values in the holes than the 3D solids and CONTS. This can be attributed to both the simplifications in the out-of-plane direction and the absence of the countersunk shape, which causes stress concentrations in the 3D solids and CONTS models. These results once again prove the importance of thermal jumps, since a temperature change of only 65 °C can lead to stresses up to 600 MPa in the bolted connections.

Moving from the 3D solids models to shells allows a computational time reduction of 50% or more. In the SLS test, the CONVS were much faster than the CONTS, whereas the opposite occurred with the wingbox subcomponent. While this may seem surprising, the reason lies in the number of elements: the SLS model using CONVS elements had 6 times fewer elements than CONTS, while for the wingbox subcomponent the reduction was only by a factor of 1.5. Given that the CONVS elements have more degrees of freedom, the time saving by the lower number of elements was offset by the increased number of degrees of freedom (see Table 2). In addition, the differences in the modelling of the contact (for instance between the virtual surfaces of the plates in the CONVS model instead of solid surfaces) may also have some influence on the computational time.

To sum up, the CONTS model is qualitatively and quantitatively close to the 3D solids model but computationally faster, and thus, presents the best trade-off between computational cost and accuracy. Although the CONVS model can capture global deformation profiles, it cannot accurately predict the changes in the clamping force as a function of the temperature, neither the load-displacement response in shear of the bolted joints. However, the CONVS model may be cheapest computationally. It is worth mentioning that, the predictions of the CONVS model could be improved by user-defined element formulations taking into account the thermal behaviour, in the out-of-plane direction, more accurately.

Future work within the frame of the INNOHYBOX project will consist of validating the CONTS approach presented here, by comparing a real subcomponent with experimental tests. After validating the model at the substructural scale, we will make use of the same approach to simulate a one-meter-long hybrid wingbox cross section, with several hundreds of bolts, and compare the results with experimental tests of the full structure. All this work will be reported in two future publications that are currently being prepared.

6. Conclusions

Taking a FEM model with 3D solid elements as the benchmark case, we have presented two simplified approaches (based on conventional shell and continuum shell elements) to simulate a large hybrid bolted assembly (carbon - aluminium) accounting for all relevant phenomenology (contacts, friction, bolt clamping load, bolt-hole clearance, thermal expansion and contraction, etc.). The simplified models have the novelty of combining beams with surface elements to model the bolts, allowing the contact of the bolt with the hole to be captured physically. In addition, the numerical approaches can capture the response of the structure including thermal effects, which are generally not considered in the literature. Two case studies of increased complexity were investigated: a simple SLS test on a coupon with one bolt and a complex wingbox subcomponent with 46 bolts under positive and negative temperature jumps.

Results show that the continuum shell model presents the best trade-off between computational time and accuracy, being qualitatively and quantitatively in good agreement with the full 3D solids model, but 13% faster with one bolt, and up to 75% faster for 46 bolts. The conventional shell model predicts similar deformed shape, displacement and stresses but fails to account for the temperature effect on the clamping force. In spite of its lack of accuracy, the conventional shell model might be the fastest if the number of elements is far fewer than in the continuum shell model.

The representation of the bolts with beam elements, the use of surface elements to account for the bolt-hole contact and the replacement of the washer with a tie constraint are proper simplifications to maintain the accuracy of the models. Moreover, a temperature excursion can significantly alter the bolt clamping force, which can lead to plate separation or bolt yielding. The shear response of the joint is also altered by the thermal loading. In summary, we have demonstrated that the modelling approach based on continuum shell elements, and the simplifications therein, is as accurate as a 3D solids model but with a much reduced computational effort, which makes it suitable for even larger structures with hundreds of bolts.

Declaration of competing interest

The authors declare that they have no known competing financial interests or personal relationships that could have appeared to influence the work reported in this paper.

Data availability

The raw/processed data required to reproduce these findings cannot be shared at this time due to legal or ethical reasons.

Acknowledgements

This work was carried out under the framework of the H2020 Clean Sky 2 Project INNOHYBOX - Innovative solutions for metallic ribs or fittings introduced in a composite box to optimally deal with thermo-mechanical effects - (Call H2020-CS2-CFP06-2017-01, reference 785433) which provided the financial support. The first author also acknowledges the Grant BES-2016-078270 from the 'Subprograma Estatal de Formación del MICINN' co-financed by the European Social Fund.

References

[1] Z. Kapidžić, L. Nilsson, H. Ansell, Conceptual studies of a composite-aluminum hybrid wing box demonstrator, Aerospace Science and Technology 32 (1) (2014) 42–50. doi:10.1016/j.ast.2013.11.002.

[2] C. Stocchi, P. Robinson, S. T. Pinho, A detailed finite element investigation of composite bolted joints with countersunk fasteners, Composites Part A: Applied Science and Manufacturing 52 (2013) 143–150. doi:10.1016/j.compositesa.2012.09.013.

[3] S. Noroozi, P. Sewell, J. Vinney, Investigation of bolt group configurations on load distribution and joint failure, Mechanics of Advanced Materials and Structures 21 (5) (2014) 422–432. doi:10.1080/15376494.2012.697604.

[4] O. Omran, V. D. Nguyen, H. Jaffal, P. Coorevits, Development of a connector element for multi-material bolted-joint under tensile loading, Mechanics of Advanced Materials and Structures 0 (0) (2018) 1–12. doi:10.1080/15376494.2018.1452314.

[5] C. Qiu, Z. Guan, S. Du, An improved characteristic length method for predicting the single bolt joint bearing strength considering secondary bending effect, Mechanics of Advanced Materials and Structures 0 (0) (2020) 1–13. doi:10.1080/15376494.2020.1821265.

[6] N. Y. Hirano, Y. Takao, W. X. Wang, Effects of temperature on the bearing strength of CF/epoxy pinned joints, Journal of Composite Materials 41 (3) (2007) 335–351. doi:10.1177/0021998306063374.

[7] C. D. Coman, D. M. Constantinescu, Temperature effects on joint strength and failure modes of hybrid aluminum–composite countersunk bolted joints, Proceedings of the Institution of Mechanical Engineers, Part L: Journal of Materials: Design and Applications 233 (11) (2019) 2204–2218. doi:10.1177/1464420719837299.

[8] E. Madenci, S. Shkarayev, B. Sergeev, D. W. Oplinger, P. Shyprykevich, Analysis of composite laminates with multiple fasteners, International Journal of Solids and Structures 35 (15) (1998) 1793–1811. doi:10.1016/S0020-7683(97)00152-2.

[9] M. A. McCarthy, V. P. Lawlor, W. F. Stanley, C. T. McCarthy, Bolt-hole clearance effects and strength criteria in single-bolt, single-lap, composite bolted joints, Composites Science and Technology 62 (10-11) (2002) 1415–1431. doi:10.1016/S0266-3538(02)00088-X.

[10] C. Girard, M. L. Dano, A. Picard, G. Gendron, Bearing behavior of mechanically fastened joints in composite laminates - Part I: Strength and Local Strains, Mechanics of Advanced Materials and Structures 10 (1) (2003) 1–21. doi:10.1080/15376490390118102.

[11] C. Girard, M. L. Dano, A. Picard, G. Gendron, Bearing behavior of mechanically fastened joints in composite laminates - Part II: Failure mechanisms, Mechan-

ics of Advanced Materials and Structures 10 (1) (2003) 23–42. doi:10.1080/15376490306738.

[12] L. Zhao, Z. Fang, F. Liu, M. Shan, J. Zhang, A modified stiffness method considering effects of hole tensile deformation on bolt load distribution in multi-bolt composite joints, Composites Part B: Engineering 171 (May) (2019) 264–271. doi:10.1016/j.compositesb.2019.05.010.

[13] X. W. Xu, H. C. Man, T. M. Yue, Strength prediction of composite laminates with multiple elliptical holes, International Journal of Solids and Structures 37 (21) (2000) 2887–2900. doi:10.1016/S0020-7683(99)00033-5.

[14] O. Zhang, J. A. Poirier, New analytical model of bolted joints, Journal of Mechanical Design, Transactions of the ASME 126 (4) (2004) 721–728. doi:10.1115/1.1760777.

[15] L. Hart-smith, Design methodology for bonded-bolted composite joints. Long beach. McDonnell Douglas Corporation, 1982.

[16] W. Nelson, B. Bunin, L. Hart-Smith, Critical joints in large composite aircraft structure. NASA CR 3710. Long Beach: McDonnell Douglas Corporation, 1983.

[17] J. Xiang, S. Zhao, D. Li, Y. Wu, An improved spring method for calculating the load distribution in multi-bolt composite joints, Composites Part B: Engineering 117 (2017) 1–8. doi:10.1016/j.compositesb.2017.02.024.

[18] C. Qiu, Z. Guan, S. Du, Z. Li, An improved model for predicting stiffness of single-lap composites bolted joints using Matlab/Simulink, Mechanics of Advanced Materials and Structures 0 (0) (2019) 1–11. doi:10.1080/15376494.2019.1675107.

[19] T. Ireman, Three-dimensional stress analysis of bolted single-lap composite joints, Composite Structures 43 (3) (1998) 195–216. doi:10.1016/S0263-8223(98)00103-2.

[20] A. Aktas, R. Karakuzu, Failure analysis of two-dimensional carbon-epoxy composite plate pinned joint, Mechanics of Composite Materials and Structures 6 (4) (1999) 347–361. doi:10.1080/107594199305502.

[21] M. L. Dano, G. Gendron, A. Picard, Stress and failure analysis of mechanically fastened joints in composite laminates, Composite Structures 50 (3) (2000) 287–296. doi:10.1016/S0263-8223(00)00119-7.

[22] K. I. Tserpes, G. Labeas, P. Papanikos, T. Kermanidis, Strength prediction of bolted joints in graphite/epoxy composite laminates, Composites Part B: Engineering 33 (7) (2002) 521–529. doi:10.1016/S1359-8368(02)00033-1.

[23] M. A. McCarthy, C. T. McCarthy, Finite element analysis of effects of clearance on single shear composite bolted joints, Plastics, Rubber and Composites 32 (2) (2003) 65–70. doi:10.1179/146580103225001390.

[24] M. A. McCarthy, C. T. McCarthy, V. P. Lawlor, W. F. Stanley, Three-dimensional finite element analysis of single-bolt, single-lap composite bolted joints: Part I - Model development and validation, Composite Structures 71 (2) (2005) 140–158. doi:10.1016/j.compstruct.2004.09.024.

[25] C. T. McCarthy, M. A. McCarthy, Three-dimensional finite element analysis of single-bolt, single-lap composite bolted joints: Part II - Effects of bolt-hole clearance, Composite Structures 71 (2) (2005) 159–175. doi:10.1016/j.compstruct.2004.09.023.

[26] C. T. McCarthy, M. A. McCarthy, V. P. Lawlor, Progressive damage analysis of multi-bolt composite joints with variable bolt-hole clearances, Composites Part B: Engineering 36 (4) (2005) 290–305. doi:10.1016/j.compositesb.2004.11.003.

[27] J. Ekh, J. Schön, Finite element modeling and optimization of load transfer in multi-fastener joints using structural elements, Composite Structures 82 (2) (2008) 245–256. doi:10.1016/j.compstruct.2007.01.005.

[28] P. J. Gray, C. T. McCarthy, A highly efficient user-defined finite element for load distribution analysis of large-scale bolted composite structures, Composites Science and Technology 71 (12) (2011) 1517–1527. doi:10.1016/j.compscitech.2011.06.011.

[29] B. Egan, C. T. McCarthy, M. A. McCarthy, P. J. Gray, R. M. Frizzell, Modelling a single-bolt countersunk composite joint using implicit and explicit finite element analysis, Computational Materials Science 64 (2012) 203–208. doi:10.1016/j.commatsci.2012.02.008.

[30] B. Mandal, A. Chakrabarti, Numerical failure assessment of multi-bolt FRP composite joints with varying sizes and preloads of bolts, Composite Structures 187 (October 2017) (2018) 169–178. doi:10.1016/j.compstruct.2017.12.048.

[31] Y. Zhang, Z. Zhou, S. Pan, Z. Tan, Comparison of failure modes and damage mechanisms of CFRP and C/C composite joints under out-of-plane loading, Mechanics of Advanced Materials and Structures 0 (0) (2020) 1–10. doi:10.1080/15376494.2020.1783404.

[32] F. Liu, W. Yao, X. Shi, L. Zhao, J. Zhang, Bearing failure optimization of composite double-lap bolted joints based on a three-step strategy marked by feasible region reduction and model decoupling, Computers, Materials and Continua 62 (2) (2020) 977–999. doi:10.32604/cmc.2020.07184.

[33] M. Shan, L. Zhao, F. Liu, D. Qi, J. Zhang, Revealing the competitive fatigue failure behaviour of CFRP-aluminum two-bolt, double-lap joints, Composite Structures 244 (February) (2020) 112166. doi:10.1016/j.compstruct.2020.112166.

[34] Y. Xiao, T. Ishikawa, Bearing strength and failure behavior of bolted composite joints (part II: Modeling and simulation), Composites Science and Technology 65 (7-8) (2005) 1032–1043. doi:10.1016/j.compscitech.2004.12.049.

[35] F. Liu, W. Yao, L. Zhao, H. Wu, X. Zhang, J. Zhang, An improved 2D finite element model for bolt load distribution analysis of composite multi-bolt single-lap joints, Composite Structures 253 (August) (2020) 112770. doi:10.1016/j.compstruct.2020.112770.

[36] V. G. Belardi, P. Fanelli, F. Vivio, A novel composite bolted joint element: Application to a single-bolted joint, Procedia Structural Integrity 12 (2018) 281–295. doi:10.1016/j.prostr.2018.11.087.

[37] V. G. Belardi, P. Fanelli, F. Vivio, FE analysis of single-bolt composite bolted joint by means of a simplified modeling technique, Procedia Structural Integrity 24 (2019) (2019) 888–897. doi:10.1016/j.prostr.2020.02.078.

[38] V. G. Belardi, P. Fanelli, F. Vivio, Theoretical definition of a new custom finite element for structural modeling of composite bolted joints, Composite Structures 258 (October 2020) (2021). doi:10.1016/j.compstruct.2020.113199.

[39] J. Kim, J. C. Yoon, B. S. Kang, Finite element analysis and modeling of structure with bolted joints, Applied Mathematical Modelling 31 (5) (2007) 895–911. doi:10.1016/j.apm.2006.03.020.

[40] Dassault Systemes/ SIMULIA, ABAQUS, Inc. ABAQUS version 6.14 Documentation. (2014).

[41] ASTM standard D 5961/D 5961M-96. Standard test method for bearing response of polymer matrix composite laminates, ASTM International, West Conshohocken, PA (1996).

[42] A. DiNicola, S. Fantle, Bearing Strength Behavior of Clearance-Fit Fastener Holes in Toughened Graphite/Epoxy Laminates, Eleventh Volume: Composite Materials—Testing and Design (1993) 220–237doi:10.1520/STP12630S.

[43] A. Sasikumar, J. M. Guerrero, A. Quintanas-Corominas, J. Costa, Numerical study to understand thermo-mechanical effects on a composite- aluminium hybrid bolted joint, Composite Structures 275 (March) (2021) 114396. doi:10.1016/j.compstruct.2021.114396.

[44] ASTM D3039 / D3039M-17. Standard Test Method for Tensile Properties of Polymer Matrix Composite Materials, ASTM International, West Conshohocken, PA (2017).
URL www.astm.org

[45] ASTM D3518 / D3518M-18. Standard Test Method for In-Plane Shear Response of Polymer Matrix Composite Materials by Tensile Test of a ±45° Laminate, ASTM

International, West Conshohocken, PA (2018).
URL www.astm.org

[46] ASTM standard E228-11. Standard Test Method for Linear Thermal Expansion of Solid Materials With a Push-Rod Dilatometer, ASTM International, West Conshohocken, PA (2011).

[47] MatWeb. Material property data. (2011).
URL http://www.matweb.com/

[48] F. S. Jumbo, I. A. Ashcroft, A. D. Crocombe, M. M. Abdel Wahab, Thermal residual stress analysis of epoxy bi-material laminates and bonded joints, International Journal of Adhesion and Adhesives 30 (7) (2010) 523–538. doi:10.1016/j.ijadhadh.2010.03.009.

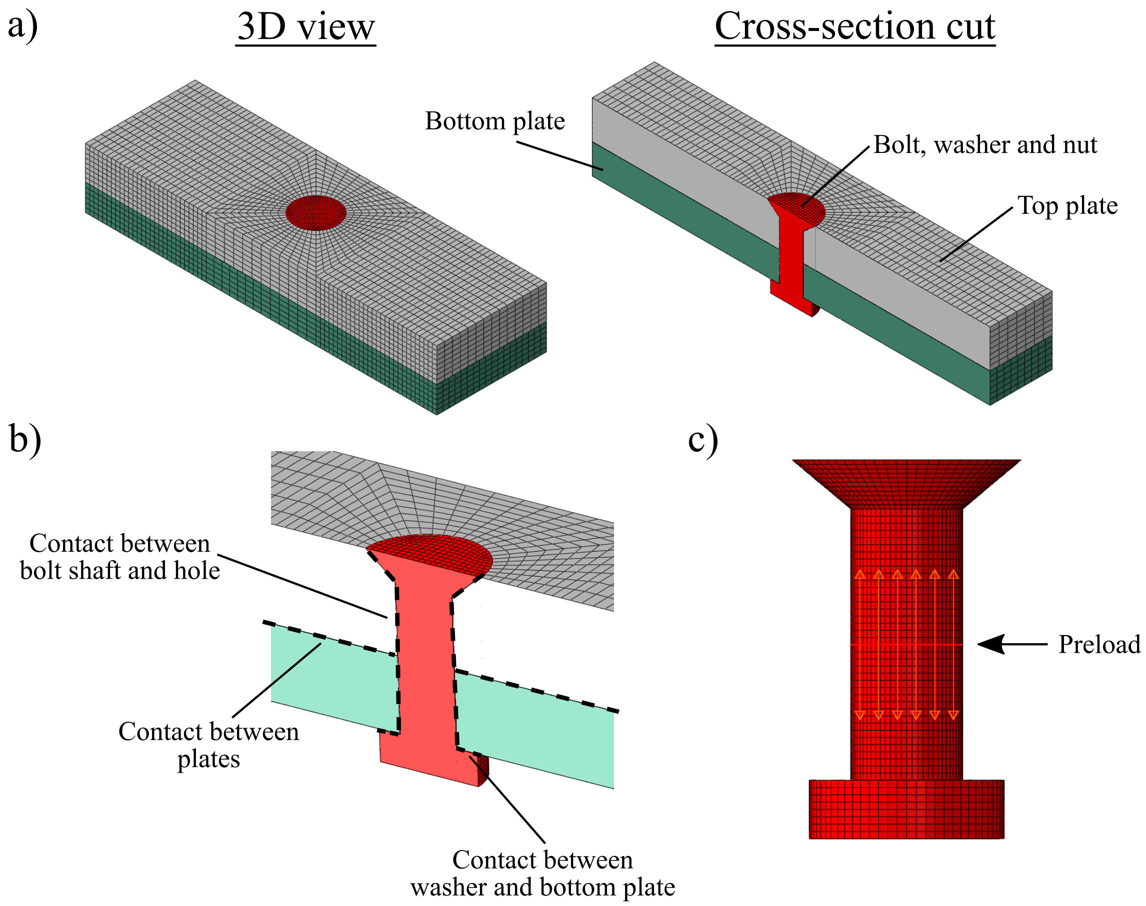

Figure 1: a) Example of two plates of different materials joined with a bolt meshed with 3D solid elements, b) contact interactions assigned to the bolted joint and c) preload given to the middle surface of the bolt.

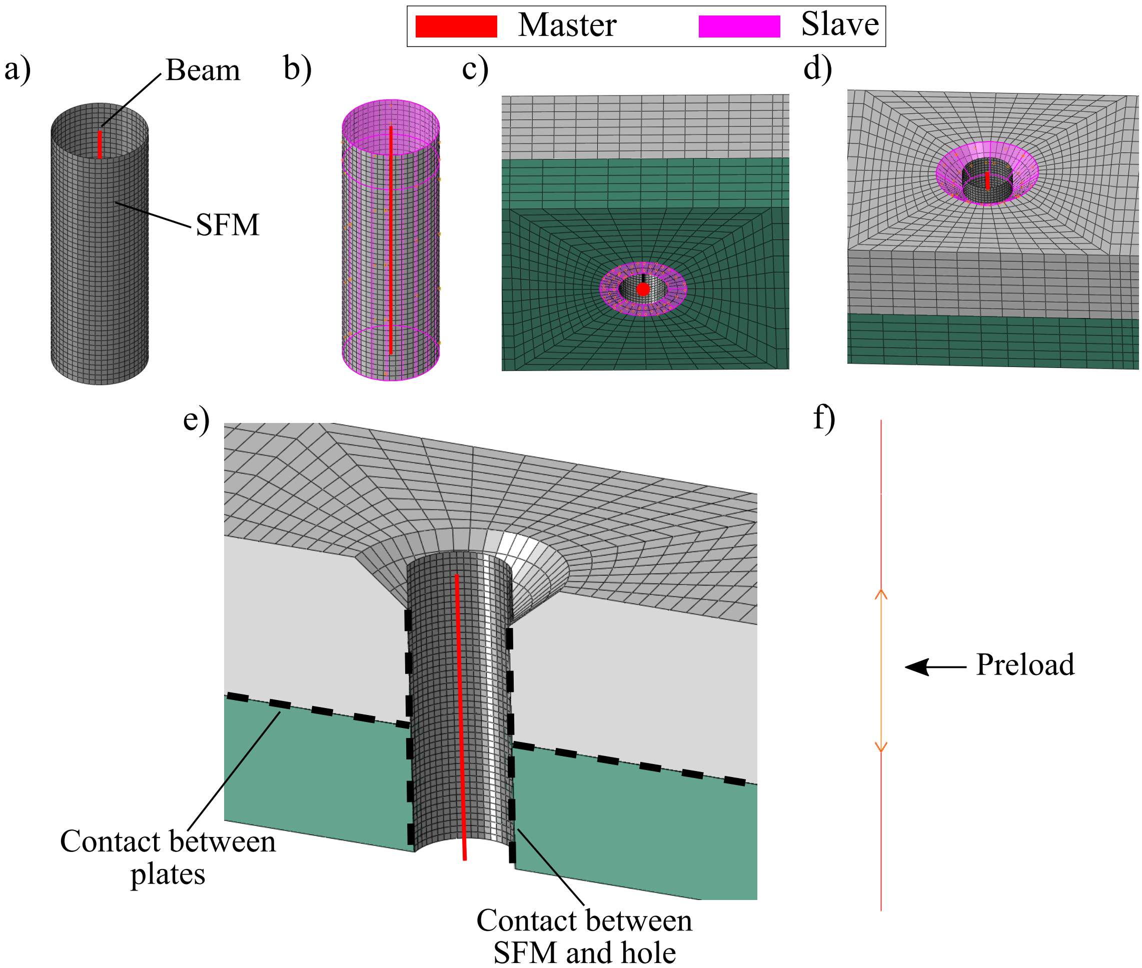

Figure 2: a) Modelling of the bolt as beam and surface elements (SFM), b) tie between the beam and the SFM, c) tie between the bottom node of the beam and the washer partition of the bottom plate, d) tie between the top nodes of the beam and the countersunk surface of the top plate, e) contact interactions and f) preload assigned to the middle element of the beam.

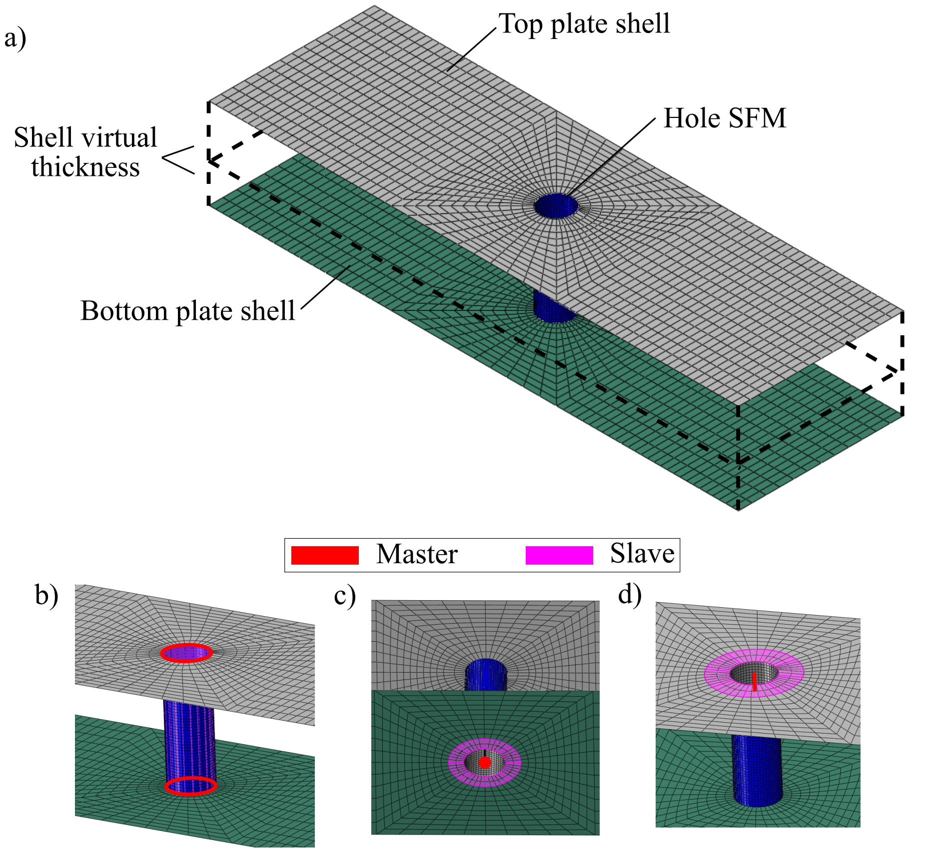

Figure 3: a) Modelling of the plates as conventional shell elements, together with surface elements (SFM) physically representing the hole of the plates, b) tie between the hole of the shells and the hole SFM, c) tie between the bottom node of the beam and the washer partition of the bottom plate and d) tie between the top nodes of the beam and the countersunk partition of the top plate.

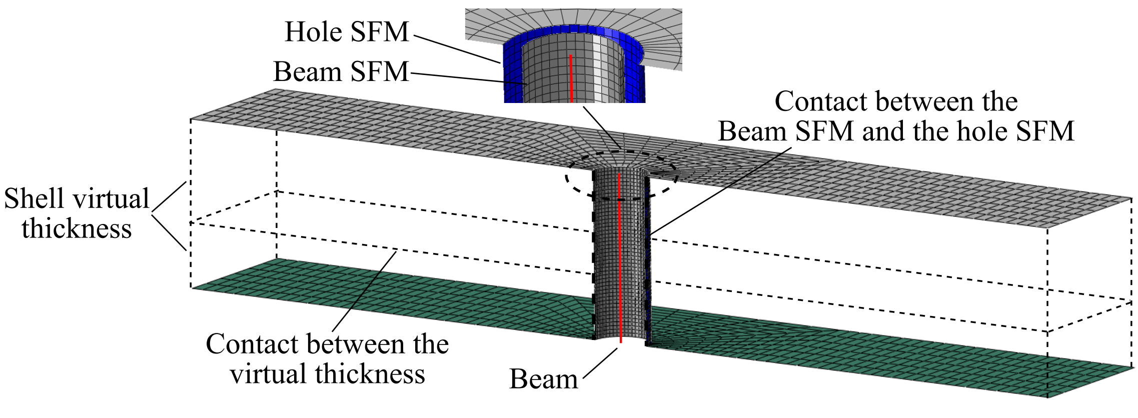

Figure 4: Contact interactions between the virtual thickness of the two plates, and between the SFM of the bolt and the SFM of the hole.

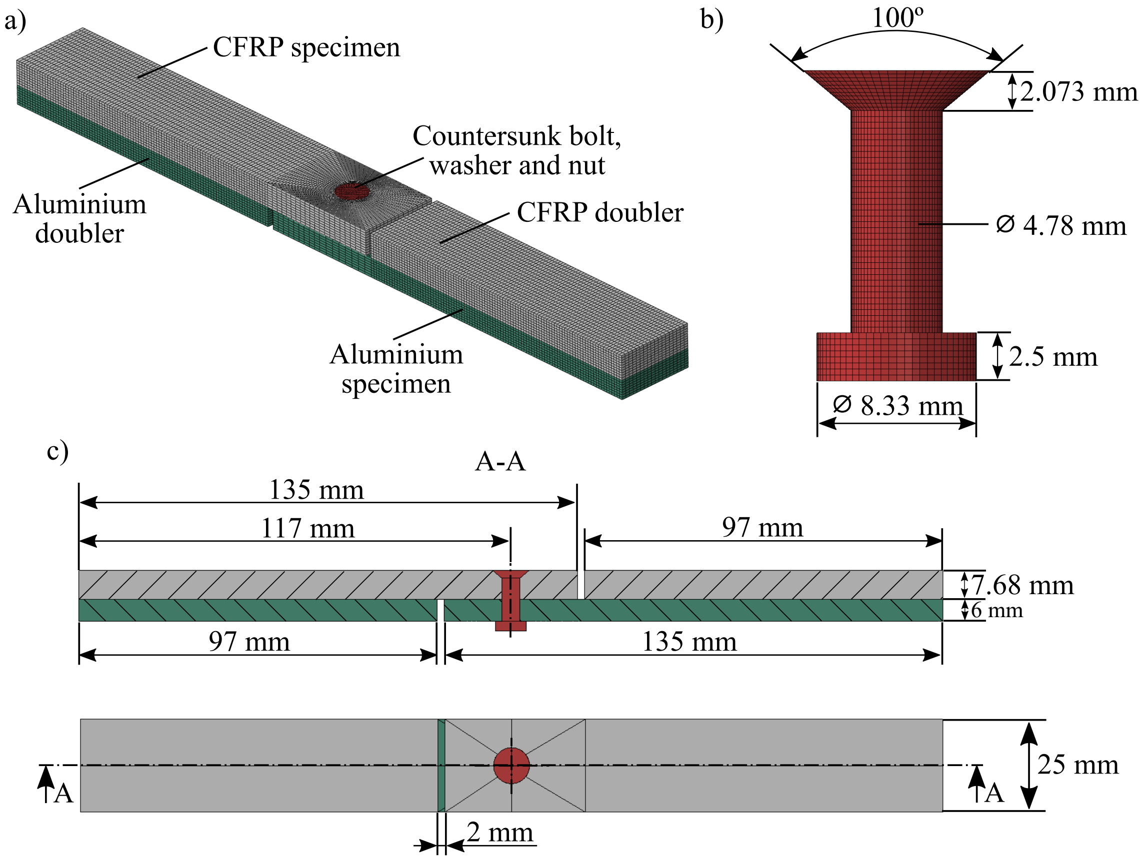

Figure 5: Representation of the single-lap shear test and geometrical details with 3D solids. a) 3D view and mesh, b) details of the bolt and c) planar view and dimensions.

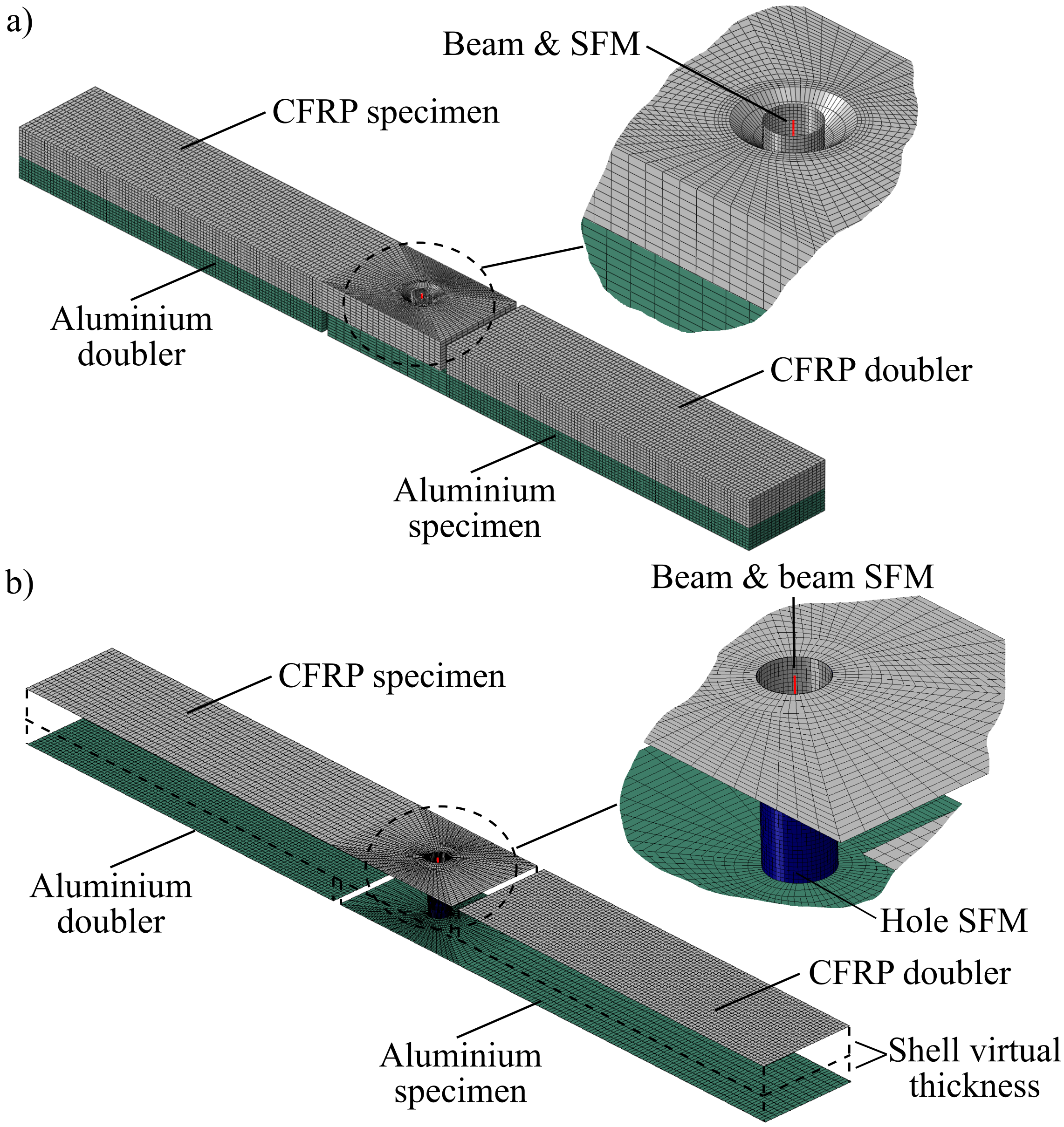

Figure 6: Representation of the single-lap shear test with the simplified methodologies. a) With continuum shells for the plates, beams and SFM for the bolt, and b) with conventional shells for the plates, SFM for the hole of the plates, and beam and SFM for the bolt.

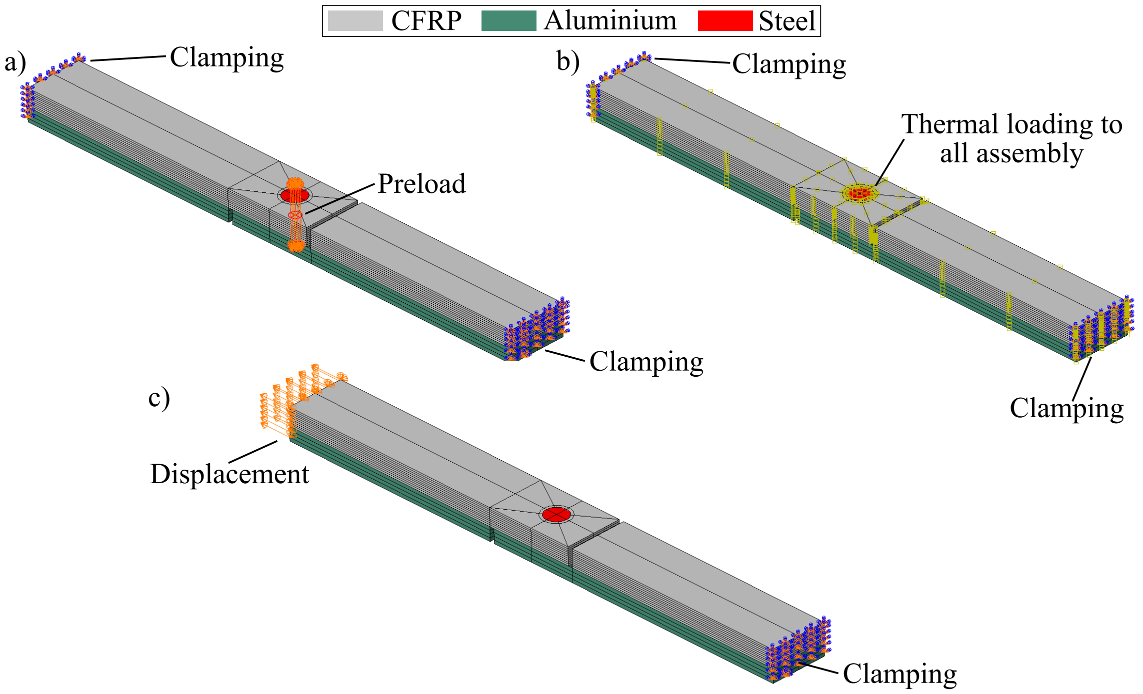

Figure 7: Representation of the boundary conditions and steps of the single-lap shear test. a) Step 1: preload, b) step 2: thermal and c) step 3: tension. The model with 3D solids is shown for easier representation.

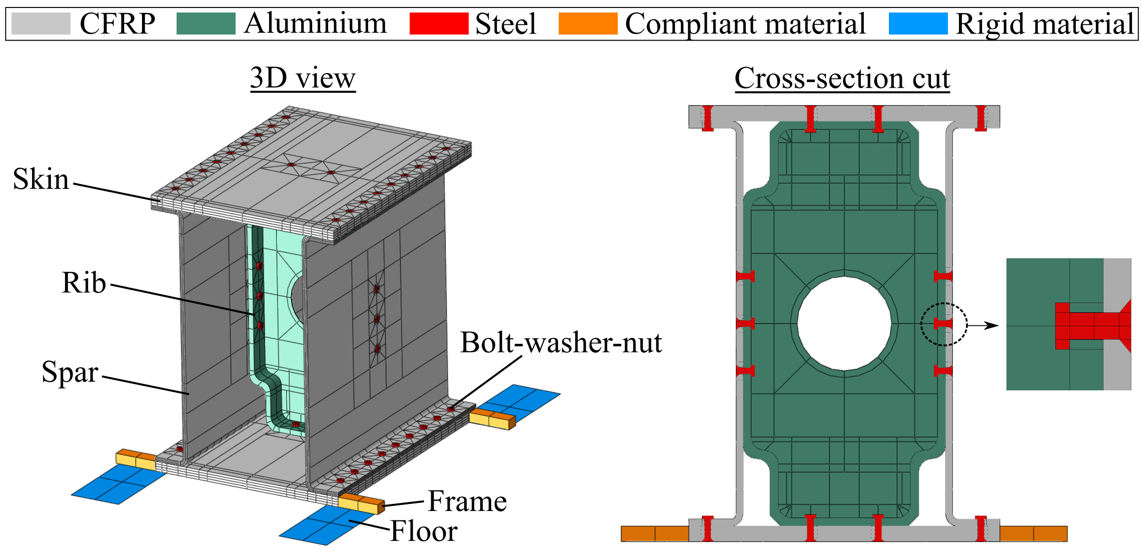

Figure 8: Wingbox subcomponent assembly and geometrical details with 3D solids.

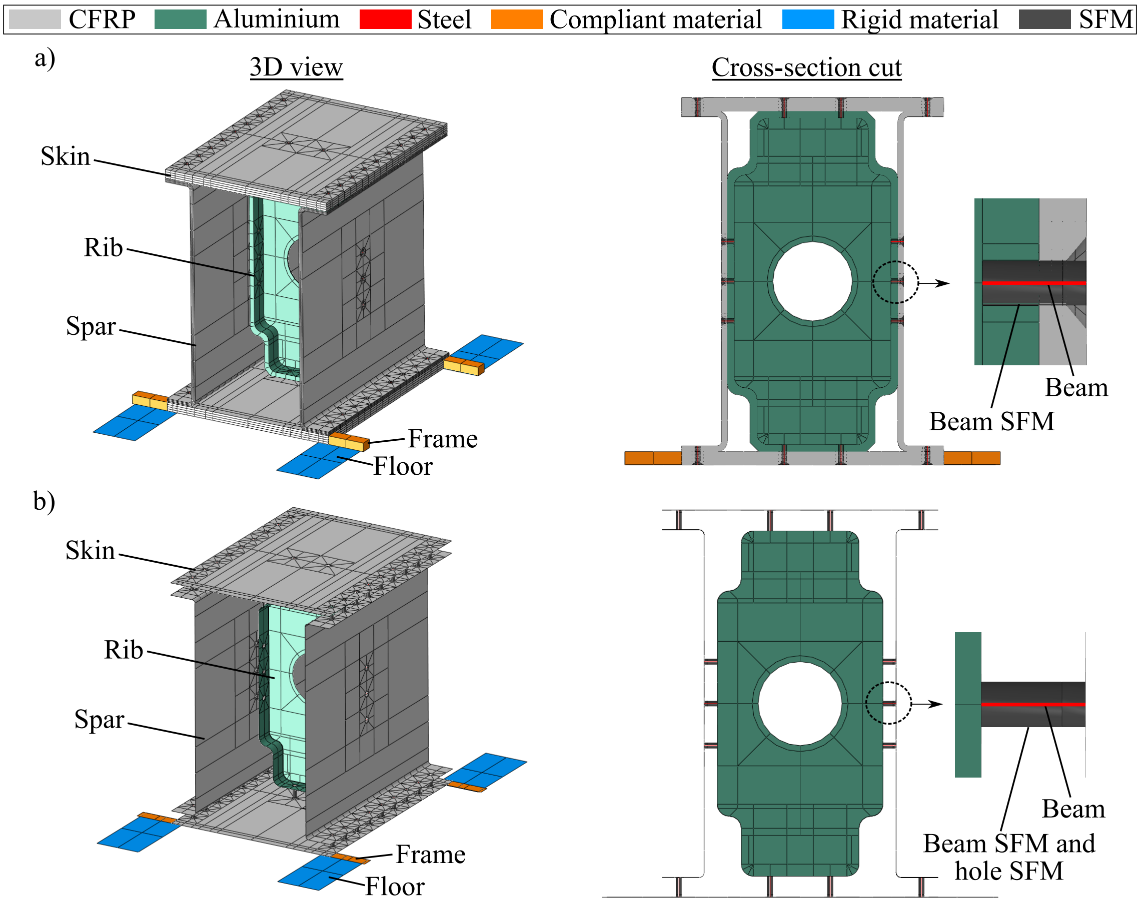

Figure 9: Wingbox subcomponent assembly with the simplified methodologies. a) With continuum shells for the rib, skins and spars, beams and SFM for the bolts, and b) with conventional shells for the rib, skins and spars, SFM for all the holes, and beam and SFM for the bolts.

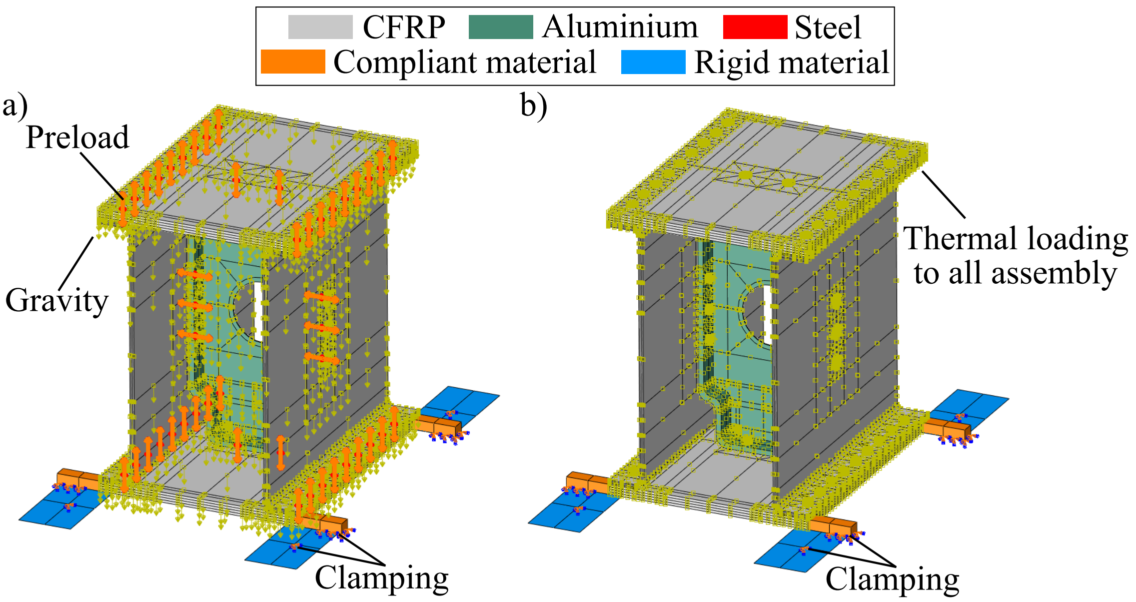

Figure 10: Representation of the boundary conditions and steps of the wingbox subcomponent simulation. a) Step 1: preload and b) step 2: thermal. The model with 3D solids is shown for easier representation.

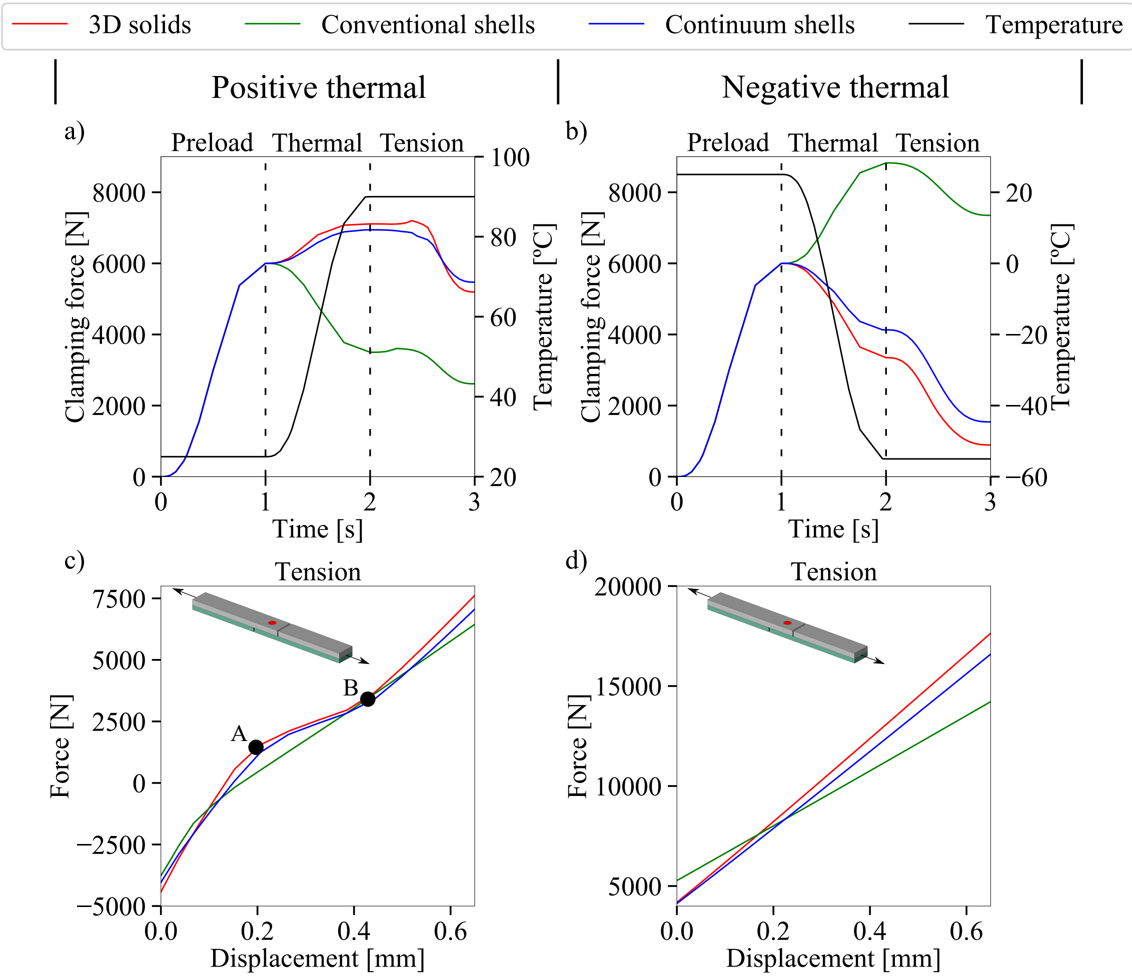

Figure 11: a)-b) Clamping force of the assembly (left Y axis) during the entire simulation (preload, thermal and tension step) and temperature evolution (right Y axis) with a positive and negative thermal step, respectively, and c)-d) force-displacement curve response obtained during step 3 (tension), with a positive and negative thermal step, respectively.

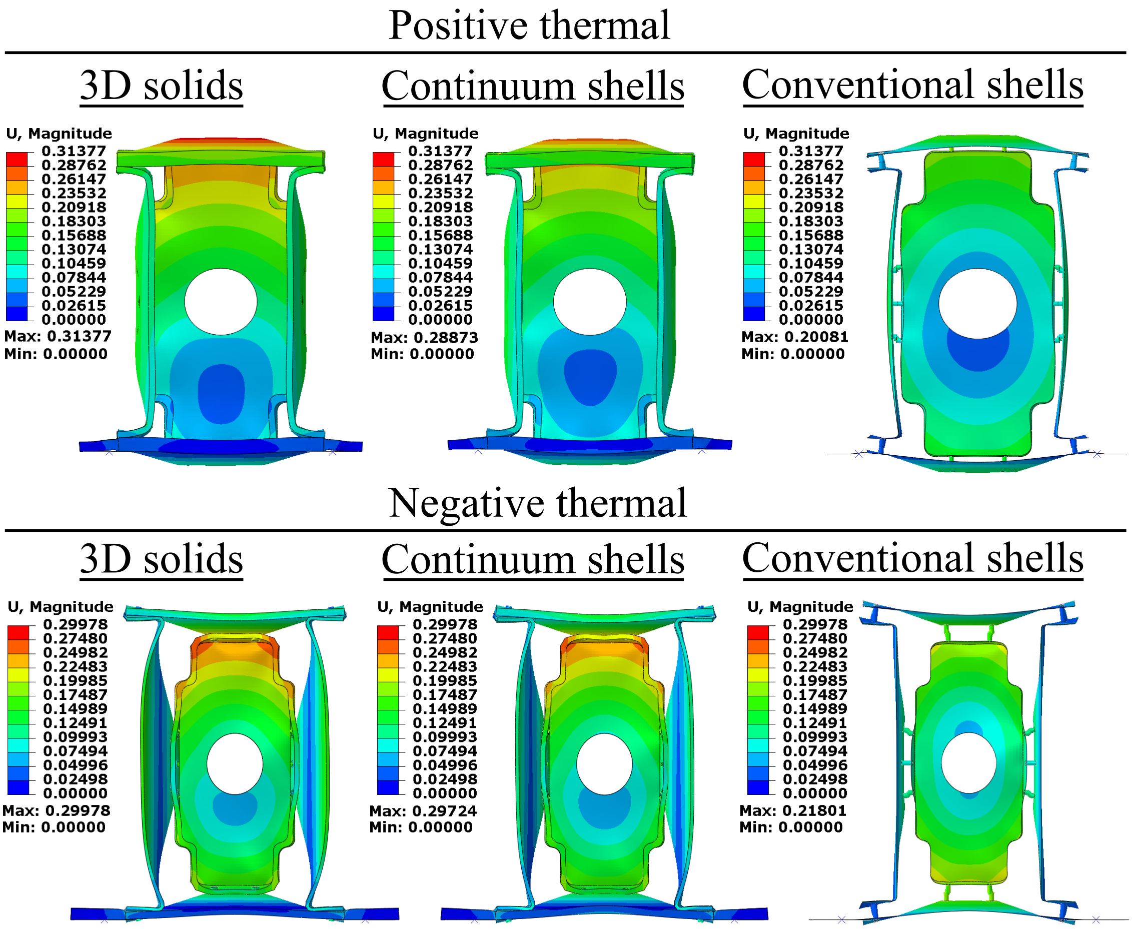

Figure 12: Displacement magnitude at the end of the thermal loading with each methodology. The deformation scale factor is 150 for the positive and 110 for the negative thermal step, respectively. The same colour scale has been used for each methodology to facilitate comparison. The actual maximum and minimum displacement of each case is also specified.

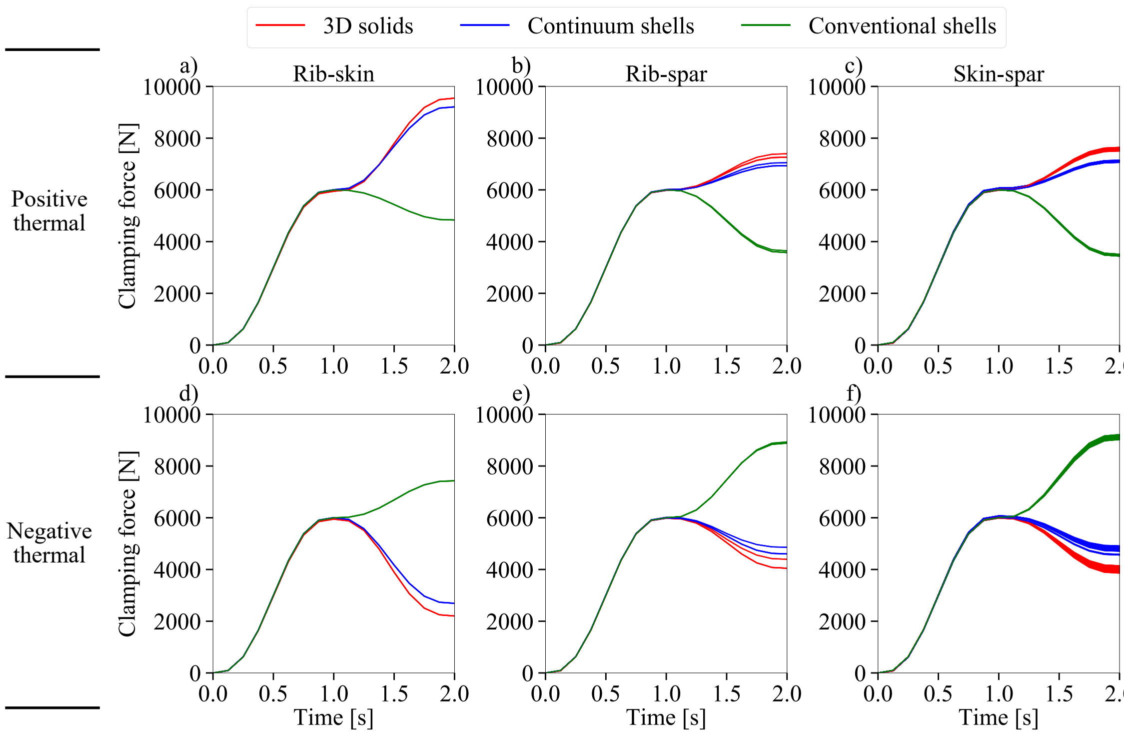

Figure 13: From a) to c), the clamping force is shown for all four bolts between rib-skin, all six bolts between rib-spar and all thirty-six bolts between skin-spar, respectively, with a positive thermal step. From d) to f), the same results are shown with a negative thermal jump. Time 0-1s corresponds to the preload, whereas time 1-2s is the thermal step.

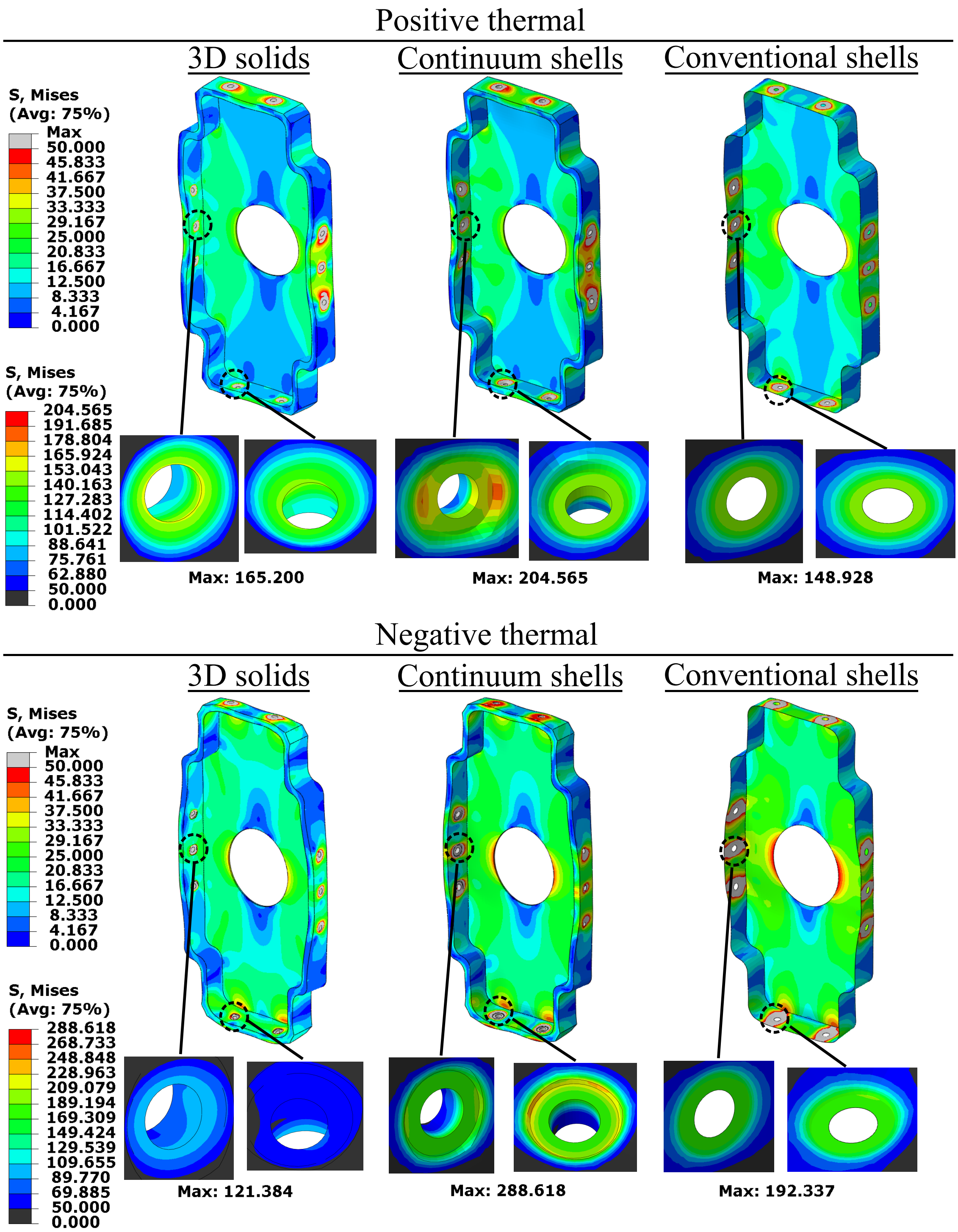

Figure 14: Von Mises stress in the rib at the end of the simulation for each methodology with a positive or negative thermal step. The deformation scale factor is 150 for the positive and 110 for the negative thermal step, respectively. The same colour scale has been used for each methodology to facilitate comparison. The actual maximum stress of each case is also specified. Notice that, for the shells, the maximum stress across all integration points in the thickness direction is shown for each element.

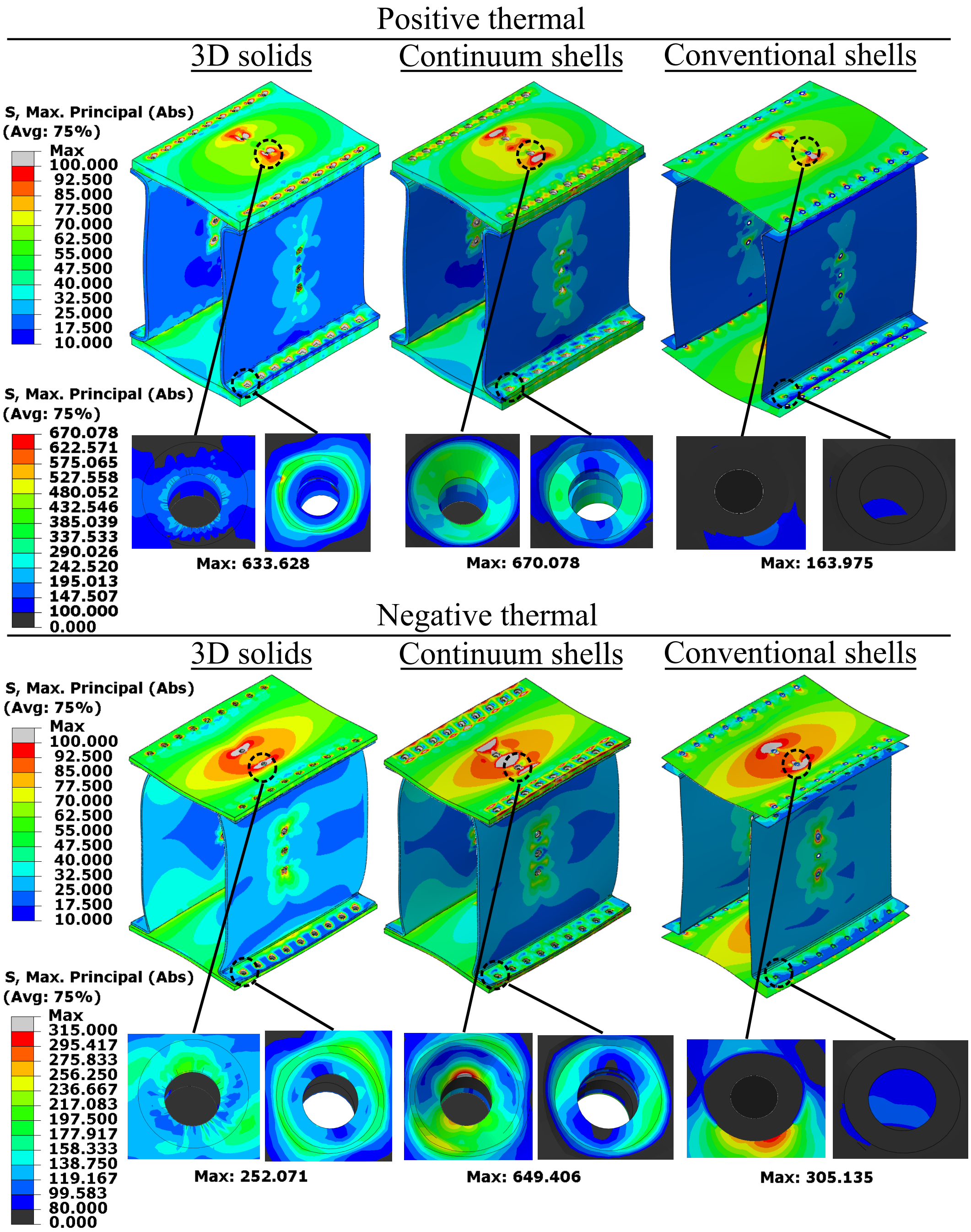

Figure 15: Maximum principal stress in the skins and spars at the end of the simulation for each methodology with a positive or negative thermal step. The deformation scale factor is 150 for the positive and 110 for the negative thermal step, respectively. The same colour scale has been used for each methodology to facilitate comparison. The actual maximum stress of each case is also specified. For each element, the maximum stress carried by all the plies contained by the element is shown.

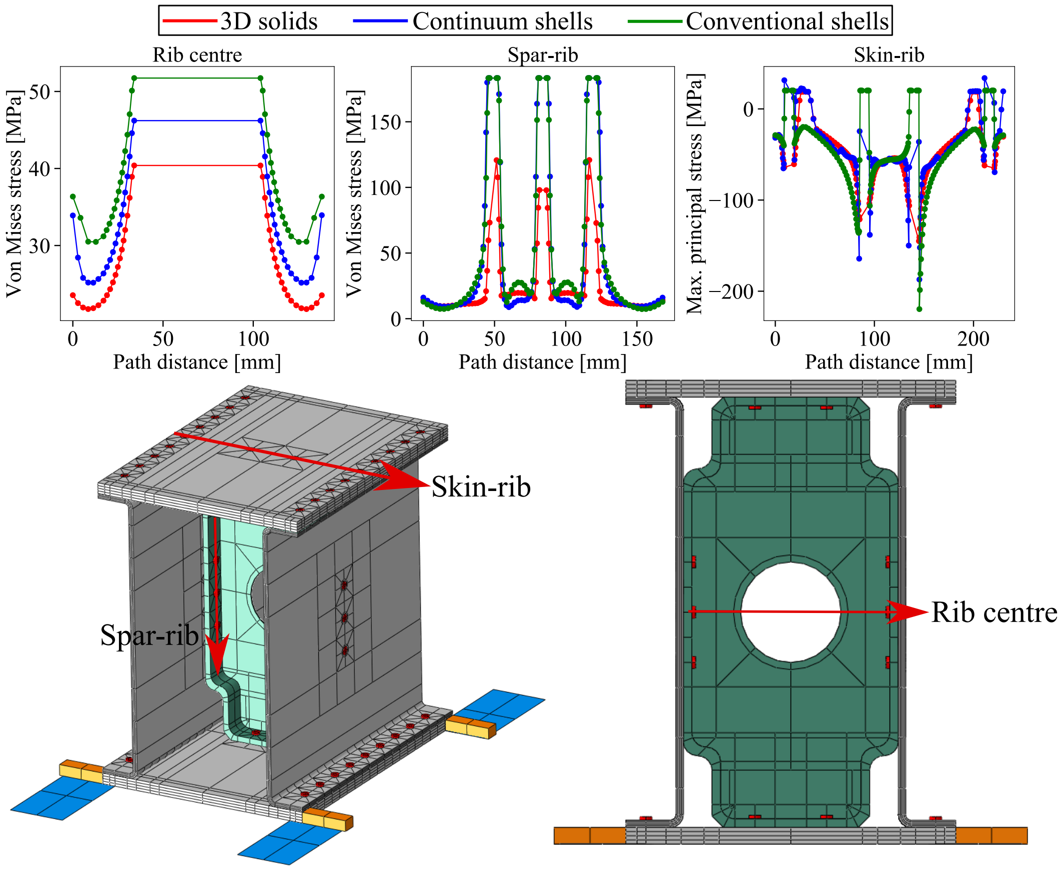

Figure 16: Stress prediction along different paths compared between the three numerical approaches under a negative thermal jump. The stress is shown along the rib central axis, the rib connection with the spar and the skin-rib bolted joints.

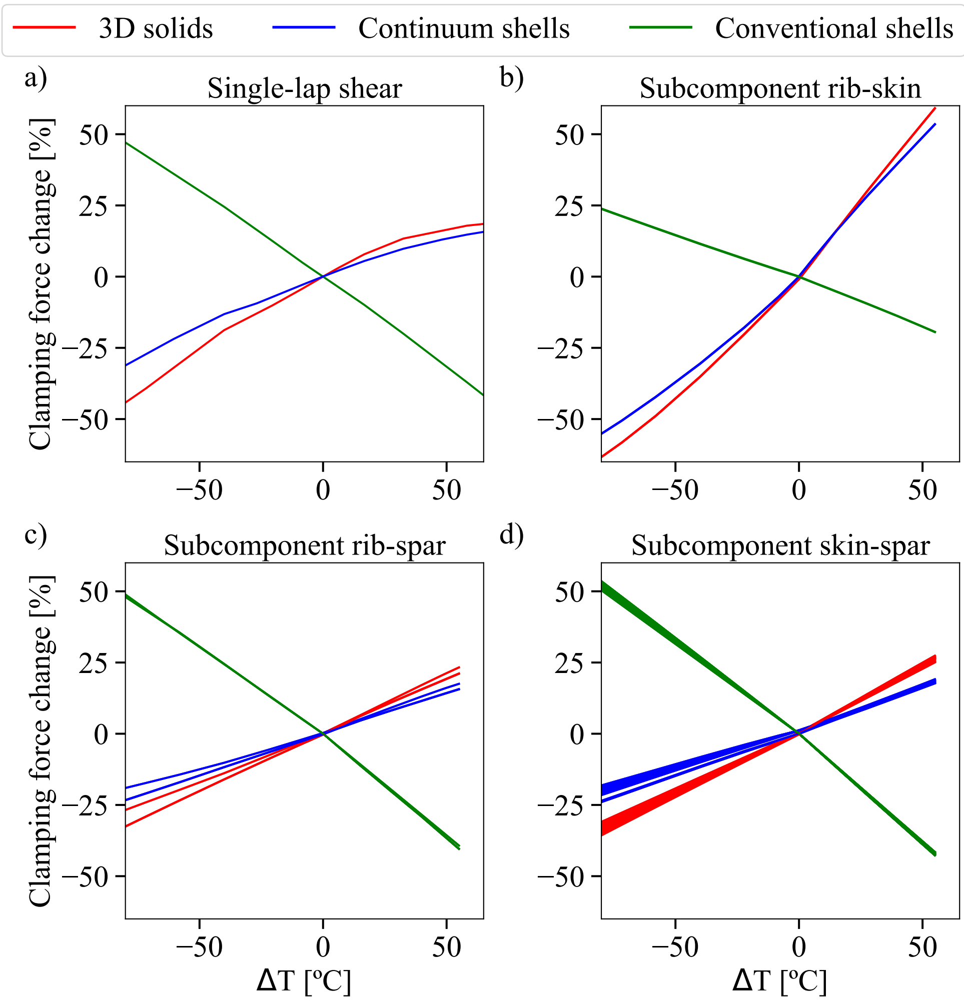

Figure 17: Percentage change of preload as a function of the temperature increment. a) For the single-lap shear bolt, b) all four bolts between rib-skin of subcomponent, c) all six bolts between rib-spar of subcomponent and d) all thirty-six bolts connecting the skin-spar of the subcomponent.

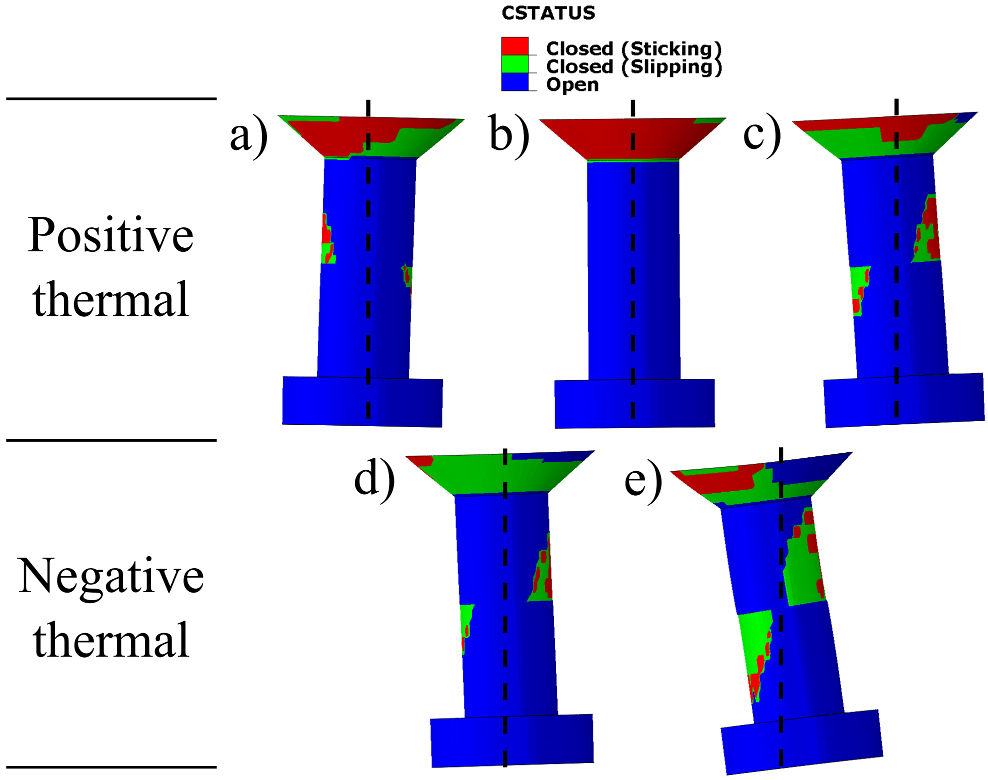

Figure 18: Bolt contact area and bending at different stages during the tensile step in the single-lap shear test with the 3D solid model. a) Beginning of tensile step with positive thermal, b) stage 2 of the load displacement response with positive thermal, c) end of the tensile step with positive thermal, d) at the beginning of the tensile step with negative thermal and e) at the end of the tensile step with negative thermal. The deformed shape factor is 2.5.

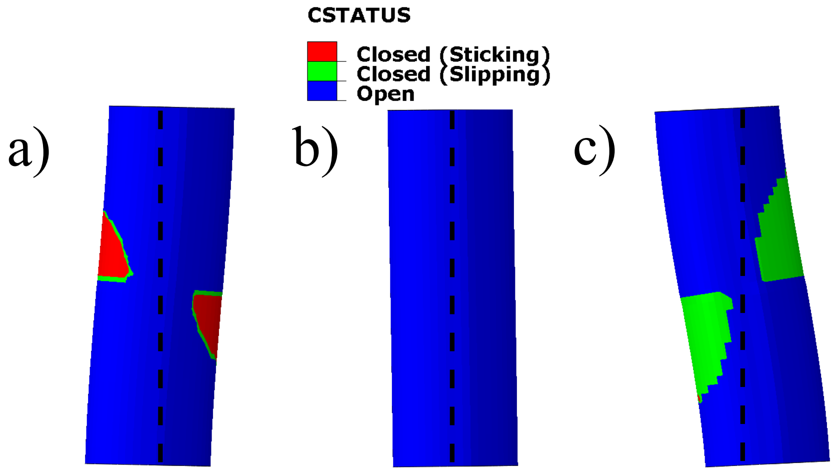

Figure 19: Bolt contact area and bending at different stages during the tensile step in the single-lap shear test with the CONVS model. a) Beginning of tensile step with positive thermal, b) stage 2 of the load displacement response with positive thermal and c) end of the tensile step with positive thermal. The deformed shape factor is 5.

Table 1: Material properties. (*) These properties were determined by means of experimental testing, following the ASTM standards D3039M, D3518M and E228-11 [44–46].

Material family	Material name	Property		Source
Steel	Steel alloy	E [MPa]	210000	[47]
		ν [-]	0.3	
		α [μm/m°C]	11	
		ρ [g/cm^3]	8	
Aluminium	Aluminium (2024-O)	E [MPa]	73100	[47]
		ν [-]	0.33	
		α [μm/m°C]	21.1	
		ρ [g/cm^3]	2.7	
CFRP	CFRP (M21 EV / IMA)	E_{11} [MPa]	165000	[48]
		E_{22} & E_{33} [MPa]	9300	Own$^{(*)}$
		ν_{12} & ν_{13} [-]	0.35	[48]
		ν_{23} [-]	0.487	Own$^{(*)}$
		G_{12} & G_{13} [MPa]	5080	Own$^{(*)}$
		G_{23} [MPa]	3127.10	$E_{22}/2\,(1+\nu_{23})$
		α_{11} [μm/m°C]	0.6	Own$^{(*)}$
		α_{22} & α_{33} [μm/m°C]	30.0	Own$^{(*)}$
		ρ [g/cm^3]	1.5	-
		Ply thickness [mm]	0.192	-

Table 2: Number of elements and computational time of each study according to the modelling approach.

Modelling approach	Single-lap shear			Wingbox subcomponent		
	Number of elements	CPU time [h:mm:ss]		Number of elements	CPU time [h:mm:ss]	
		Positive thermal	Negative thermal		Positive thermal	Negative thermal
3D solids	111978	0:38:20	0:40:34	701968	9:20:24	10:01:30
Continuum shells	92974	0:33:59	0:37:12	573138	2:35:18	2:35:51
Conventional shells	15087	0:17:13	0:15:46	362510	5:08:32	4:57:17